Structural and Optical Properties of Molecular Beam Epitaxy Grown InAsBi Bulk Layers and Quantum Wells

by

Arvind Joshua Jaydev Shalindar Christraj

A Thesis Presented in Partial Fulfillment
of the Requirements for the Degree
Master of Science

Approved July 2016 by the
Graduate Supervisory Committee:

Shane R. Johnson, Chair
Terry L. Alford
Michael Goryll

ARIZONA STATE UNIVERSITY

August 2016

ABSTRACT

InAsBi is a narrow direct gap III-V semiconductor that has recently attracted considerable attention because its bandgap is tunable over a wide range of mid- and long-wave infrared wavelengths for optoelectronic applications. Furthermore, InAsBi can be integrated with other III-V materials and is potentially an alternative to commercial II-VI photodetector materials such as HgCdTe.

Several 1 μm thick, nearly lattice-matched InAsBi layers grown on GaSb are examined using Rutherford backscattering spectrometry and X-ray diffraction. Random Rutherford backscattering measurements indicate that the average Bi mole fraction ranges from 0.0503 to 0.0645 for the sample set, and ion channeling measurements indicate that the Bi atoms are substitutional. The X-ray diffraction measurements show a diffraction sideband near the main (004) diffraction peak, indicating that the Bi mole fraction is not laterally uniform in the layer. The average out-of-plane tetragonal distortion is determined by modeling the main and sideband diffraction peaks, from which the average unstrained lattice constant of each sample is determined. By comparing the Bi mole fraction measured by random Rutherford backscattering with the InAsBi lattice constant for the sample set, the lattice constant of zinc blende InBi is determined to be 6.6107 Å.

Several InAsBi quantum wells tensilely strained to the GaSb lattice constant with dilute quantities of Bi are characterized using photoluminescence spectroscopy. Investigation of the integrated intensity as a function of carrier excitation density spanning 5×10^{25} to 5×10^{26} cm^{-3} s^{-1} indicates radiative dominated recombination and high

quantum efficiency over the 12 to 250 K temperature range. The bandgap of InAsBi is ascertained from the photoluminescence spectra and parameterized as a function of temperature using the Einstein single oscillator model. The dilute Bi mole fraction of the InAsBi quantum wells is determined by comparing the measured bandgap energy to that predicted by the valence band anticrossing model. The Bi mole fraction determined by photoluminescence agrees reasonably well with that estimated using secondary ion mass spectrometry.

DEDICATION

This work is dedicated to my parents Banu and Shailu who supported me all my life and enabled me to pursue my education in the USA.

ACKNOWLEDGMENTS

I would like express my gratitude to my advisor Dr. Shane Johnson for enabling me to work on this research. Most importantly, I learnt from him the value of critical thinking and effective writing.

I would like to thank my committee members Dr. Terry Alford and Dr. Michael Goryll for the time and effort they put into this work.

Many thanks are due to my friends and colleagues who helped familiarize me with my research; namely, Dr. Preston Webster (who grew all the samples studied), Nate Riordan, Chaturvedi Gogineni, Barry Wilkens, and Mark Mangus. To the members of the research groups of Professors Yong-Hang Zhang, David Smith, Nathaniel Newman, Terry Alford, Jeff Drucker, and Dr. Peter Williams, Dr. Klaus Franzreb, Dr. Emmanuel Soignard, and Dr. Lynda Williams, I would like to express my thanks for their assistance.

I owe special thanks to my parents, my brother Abishek, my uncle Ari, my aunt Sandra, and my friends Dharav Shah, Ashraf Ali, Eyni Gurunaathan, Geo Wilfred, Joel Terry, Aditya Yerramilli, Diana Joseph, Shriram Thamodharan, Tiffany Wingerson, Susan Terkelsen, Raja and Anupama Raman, Raju Pusapati, Meera Sridhar, Evangeline Chilka, Alice Jeevanandam, N. Narayanan, Sheethal Preethi, and D. Karunanidhi for emotionally supporting me during the past four years.

I gratefully acknowledge financial support through the National Science Foundation, Grant No. DMR-1410393. I gratefully acknowledge the use of facilities in the LeRoy Eyring Center for Solid State Science and the John M. Cowley Center for High Resolution Microscopy at Arizona State University.

TABLE OF CONTENTS

Page

LIST OF TABLES

LIST OF FIGURES

Figure Page

LIST OF ABBREVIATIONS

RBS Rutherford Backscattering Spectrometry

XRD X-Ray Diffraction

PL Photoluminescence

SIMS Secondary Ion Mass Spectrometry

1 INTRODUCTION

Optoelectronics is the branch of semiconductor electronics that deals with devices that generate or detect light. Over the past few decades, there has been a demand for new materials for mid- and long-wavelength infrared optoelectronic devices such as photodetectors and emitters for communication, defense, medical, and gas-sensing applications. Ideally, commercial free-space communication devices are designed to operate in the mid- (3-5 μm) and long-wavelength (8-12 μm) infrared atmospheric transmission windows since these windows offer low atmospheric signal attenuation; see Fig. 1.

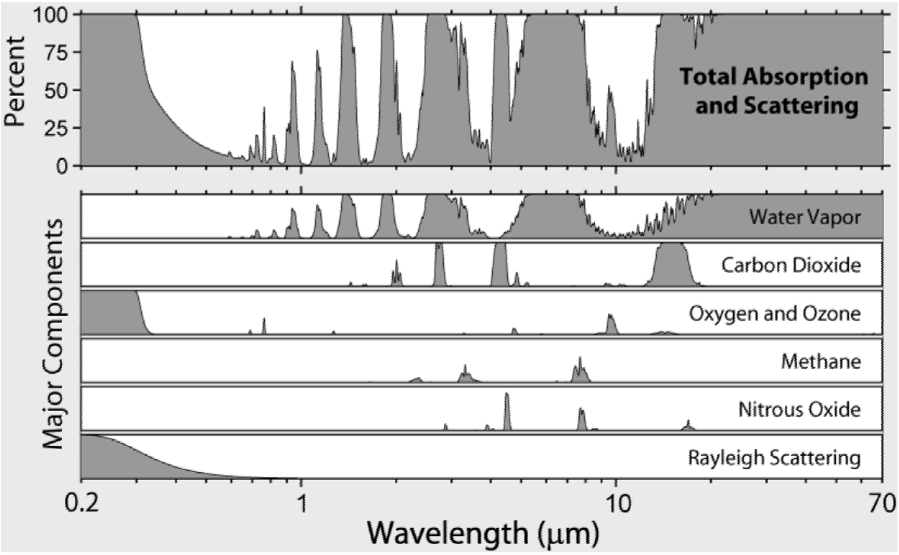

Figure 1: Atmospheric transmission spectrum of radiation. Courtesy: Robert A. Rohde / Global Warming Art. [1]

Infrared countermeasures protect military aircraft from incoming heat-seeking missiles by functioning as a strong infrared radiation source that distracts the missile

guidance system away from the aircraft engine. Infrared vision security cameras image objects even under low light conditions by detecting thermal radiation. Several medical devices make use of the abundance of important absorption and emission lines present in the infrared wavelength region. For example the 2.9 μm infrared radiation line corresponds to a maximum in the absorption spectrum of water and is therefore suitable for imaging human tissues. Similarly, the strong glucose absorption line at 2.5 μm is used in live cell imaging. Gas detectors are designed to detect strong emission lines for respiratory hazards such as carbon dioxide, methane and carbon monoxide present in the mid- and long-wavelength infrared ranges. All industry-grade commercial pyrometers operate at 2.7 μm.

The defining parameter of an optoelectronic semiconductor is its bandgap energy (E_g), which is the minimum photon energy required to excite an electron from the highest the valance band energy to the lowest conduction band energy. The active region of a photodetector absorbs photons having energies at and above E_g and is transparent to photons having energies below E_g. The following expression provides the relationship between the operation wavelength of an optoelectronic device λ_g and active material bandgap E_g

$$\lambda_g(\mu m) = \frac{h\ (eV\ s) \times c(m\ s^{-1})}{E_g(eV)} = \frac{1.24\ (eV\ \mu m)}{E_g(eV)} \tag{1.1}$$

where, $h = 4.136\times10^{-15}$ eV s is the Planck's constant and $c = 2.997$ m s^{-1} is the speed of light in vacuum. From Equation 1.1, it is clear that high-quality narrow bandgap direct semiconductors are desirable for efficient detection and emission in the infrared.

A section of the periodic table is shown in Fig. 2. Direct bandgap II-VI materials offer full flexibility to cover the infrared range through alloying suitable II-VI binary semiconductors such as CdTe and ZnTe with controlled amounts of negative-bandgap semimetals such as HgTe and HgSe. HgCdTe is the most prominently used II-VI semiconductor and has been studied since the 1960s as its composition can be tuned to cover the optical spectral range of 1-20 μm [2]. II-VI semiconductors with temperature-independent bandgaps that do not require cooling, such as $Hg_{0.4}Cd_{0.6}Te$, are well suited for telecommunication lasers. However, narrow bandgap II-VI semiconductors are not easily integrated with electronic devices; moreover they contain highly toxic Hg (mercury). This motivates research of mercury-free III-V alloys, which are easily integrated with electronic devices for mid- and far-wavelength optoelectronic devices.

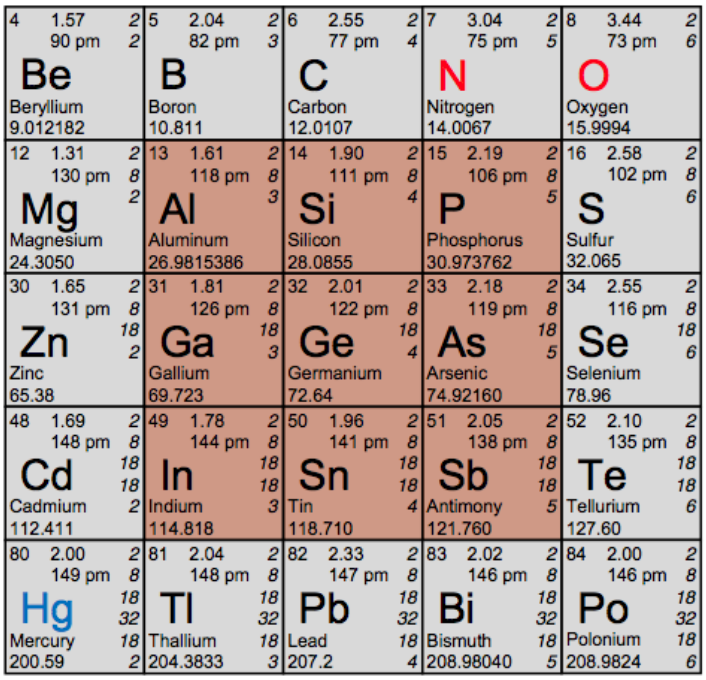

Figure 2: A section of the periodic table representing elements commonly used as semiconductors. The atomic number (*49*), electronegativity value (*1.78*), covalent radius (*144 pm*), electronic configuration (*2, 8, 18, 18, 3*), element symbol (*In*), element name (*Indium*), and atomic mass (*114.818*) are shown for every element. *Courtesy*: Chaturvedi Gogineni.

The bandgap energy of selected III-V semiconductors is plotted as a function of the lattice constant in Fig. 3a at low temperature and 3b at room temperature; the data points are solid black circles (solid black squares) for direct (indirect) bandgap materials [3]. A wide, continuous spectral range of direct bandgaps from the low energy visible to the long-wavelength infrared is accessible by using III-V ternary alloys (see solid curves). However, only a handful of these compositions can be grown with high epitaxial quality due to a limited number of commercial lattice-matched substrates being available; including GaAs, InP, and GaSb. For example, of all InAsSb ternary compositions (blue

curve, Figure 3) $InAs_{0.39}Sb_{0.71}$ has the narrowest bandgap, 138 meV (9 μm) for at 77 K [4], but suffers the lack of easily available substrates for nearly lattice-matched growth.

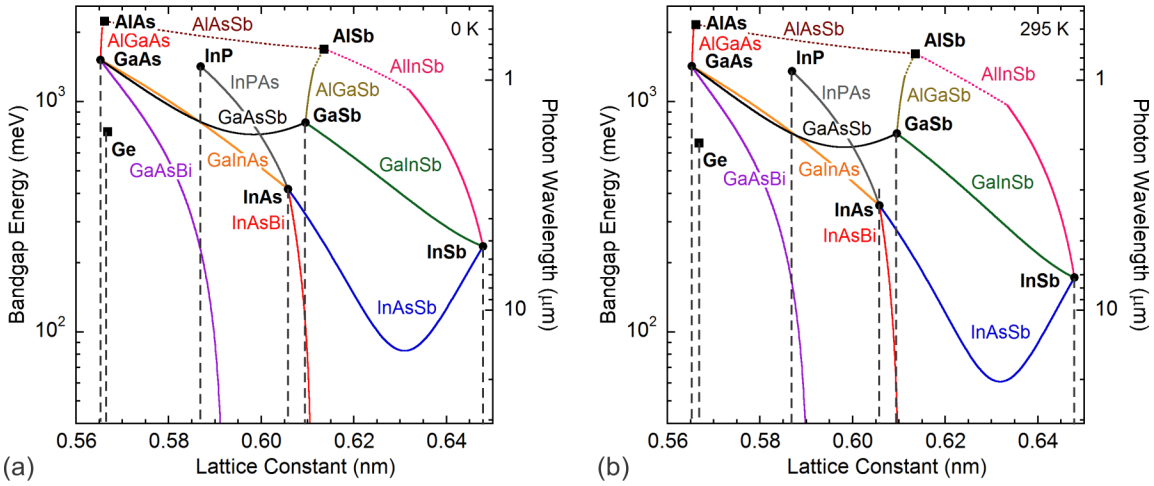

Figure 3: Bandgap energy as a function of the lattice constant of III-V semiconductors at (a) low temperature and (b) room temperature. Direct bandgap binary and ternary alloys are indicated with circles and solid curves and indirect bandgap materials are indicated with squares and dotted curves respectively. The lattice constants of common binary substrates are indicated with vertical dashed lines.

During the growth of highly strained epilayers, the layer thickness must be limited as a precaution against lattice relaxation. Otherwise, the layer may relax through the formation of lattice defects [5] that can increase the shot noise in the detector or even degrade the device beyond operability. On the other hand, limiting the strained layer thickness can restrict the amount of light absorbed and lead to deterioration of the signal to noise ratio. Therefore minimizing material strain is an important design consideration for high-performance optoelectronic devices.

Historically, the development of new semiconductor materials has had tremendous impact on technology. For example, breakthroughs in the research of III-V nitride semiconductor materials paved the way for vast improvements in commercial solid-state lighting. Only a few decades before these breakthroughs, nitride semiconductors did not receive much attention in materials research. This example leads to the question of whether there are further opportunities for the development of III-V optoelectronic materials that may have been overlooked. Bi (bismuth) and Th (thallium) are two of the least studied group III-V elements. Bismuth is a naturally occurring, stable, non-radioactive element that is relatively non-toxic when compared to mercury (Hg), thallium (Tl), antimony (Sb), lead (Pb) and polonium (Po); incidentally, bismuth is the active ingredient in some pharmaceuticals. Thallium, on the other hand, is more toxic than bismuth, and even arsenic. Bismuth has the largest covalent radius of all group-V elements. For the past few decades, bismuth has been alloyed with conventional III-V semiconductors and its effect on the material electronic bandstructure has been studied.

The ternary alloy InAsBi (red curve, Fig. 3) provides a means of reaching wavelengths in the mid- (3-5 μm) and long-wave (8-12 μm) infrared atmospheric transmission windows, similar to InAsSb. In these ternary alloy systems, the larger atomic radius and smaller electronegativity of the incorporated Bi or Sb atoms produces an upward shift in the valence band, which acts to strongly reduce the bandgap energy of the material [6]. This effect is stronger in InAsBi than in InAsSb mainly because Bi is the largest, least electronegative group-V atom. The conduction band is shifted downward in InAsBi due to a type-I alignment between InAs and semimetallic InBi [7] and upward in InAsSb due to type-II alignment between InAs and InSb [8]; this

difference as well contributes to the larger bandgap reduction observed in InAsBi. In particular, Bi reduces the bandgap of bulk InAsBi at an average rate of 55 meV/% Bi at low temperature and 51 meV/% Bi at room temperature, [9,3] whereas Sb reduces the bandgap of bulk InAsSb at average rates of 11.2 meV/% Sb at low temperature and 9.3 meV/% Sb at room temperature [8].

The reported values of the InBi lattice constant range from 6.500 Å to 7.292 Å, [6,10-15] with an average value around 6.896 Å, which is not much greater than the 6.4794 Å InSb lattice constant [16]. As a result, the strain introduced by the incorporation of Bi in InAs is not significantly greater than that introduced by the Sb in InAs, and the subsequent InAsBi bandgap reduction rate in terms of strain is significantly greater than for InAsSb. Thus the addition of Bi to the 6.1 Å GaSb and InAs material mix is particularly appealing for highly tunable low-strain optoelectronic device applications.

In this work, the structural properties of nearly lattice-matched InAsBi on GaSb are examined using Rutherford backscattering spectrometry and X-ray diffraction in Chapter 2 and using ion channeling in Chapter 3. The optical properties of InAsBi quantum wells tensilely strained to the GaSb lattice constant with dilute quantities of Bi are investigated using photoluminescence spectroscopy in Chapter 4.

2 MEASUREMENT OF InAsBi MOLE FRACTION AND INBI LATTICE CONSTANT

Random Rutherford backscattering spectrometry is used to determine the concentration of the heavy Bi atoms present in the matrix of lighter In and As atoms. X-ray diffraction is used to determine the tetragonal distortion of the InAsBi lattice, from which the InAsBi lattice constant is inferred. From these results the InAsBi lattice constant as a function of Bi mole fraction is determined.

2.1. Samples Studied

Nearly lattice-matched, 1 μm thick InAsBi layers are grown on GaSb substrates by molecular beam epitaxy with growth temperatures ranging from 270 to 280 °C, Bi/In flux ratios ranging from 0.060 to 0.065, and As/In flux ratios ranging from 0.98 to 1.02 [7]. The samples studied are high-quality epitaxial material with no Bi droplets on the surface; the growth conditions for each sample are provided in Table I. These samples nominally consist of a 500 nm thick GaSb buffer layer, a 15 nm thick InAs layer, a 1000 nm thick InAsBi layer, and a 10 nm InAs cap, except for Sample f that is instead capped with 10 nm of GaSb and Sample g that is uncapped.

Table I: Bulk InAsBi sample growth temperature and V/III flux ratios.

Sample	Growth temperature (°C)	Bi/In flux ratio	As/In flux ratio
a	280	0.065	0.96
b	270	0.065	0.96
c	270	0.065	1.00
d	280	0.060	1.00
e	280	0.060	1.03
f	280	0.060	1.00
g	280	0.060	1.05

2.2. Random Rutherford Backscattering Spectrometry

In 1911, Ernest Rutherford observed that when a thin gold foil is placed in the path of an accelerated beam of helium ions, most of the ions passed through the foil undeflected. However, a small fraction of the ions were scattered at very large angles or *backscattered*. Based on this, Rutherford proposed the nuclear model of the atom postulating that while most of the atom is empty, there is a high concentration of positively charged mass at the center of the atom and called this mass the atomic nucleus. The gold nuclei are responsible for backscattering some of the beam ions.

Rutherford backscattering spectrometry (RBS) is an ion beam analysis technique based on collisions between a homogeneous mono-energetic beam of particles having a small mass number and accelerated to a few MeV and the atomic nuclei in the target sample. The loss in kinetic energy of a projectile ion during backscattering at angles near 170° by energy transfer to a heavier, stationary target nucleus at a certain depth in the sample depends on (i) the mass of the target atom and (ii) the depth at which the

scattering takes place. As this energy loss by large angle scattering is well understood, the mole fraction and depth profile of a sample can be obtained using RBS [17]. The sample is placed in a vacuum chamber during RBS measurements to minimize scattering by gases in the atmosphere.

During the characterization of a crystalline sample using RBS, the ion beam is aligned off-axis to high-symmetry crystal directions to ensure that the majority of atoms up to a depth of a few microns are probed by the ion beam. This ensures that the atoms in the crystal appear random to the incident ion beam; therefore the characterization technique is called random RBS. On the other hand, alignment of the ion beam on-axis with a high-symmetry crystal direction results in ion-channeling, which is discussed in the Chapter 3.

The use of projectile nuclei accelerated to sharply defined energies in the > 5 MeV regime can lead to nuclear reactions with the target atoms, the analysis of which is complicated. However, random RBS typically utilizes incident particles of energies < 4 MeV and is explained using classical mechanics [17].

During backscattering experiments, the distance of closest approach of the helium ion is in most cases within the electronic orbit of the target atom. Stopping power of a medium is a term that describes the loss of kinetic energy of charged particles passing through the medium [18]. Stopping power $S(E)$ of the material through which the projectile ion is traveling is defined as the energy loss per unit path length, x as shown in Equation 2.1 and has units of energy per unit length.

$$S(E) = -dE/dx \tag{2.1}$$

A light ion slowing down in a lattice of heavy materials is subjected to electronic and nuclear stopping forces. Electronic stopping refers to the slowing down of the ion due to the inelastic collisions between bound electrons in the medium and the ion moving thorough it that may result both in excitations of bound electrons of the medium, and in excitations of the electron cloud of the ion. Considering the electronic stopping power as momentum transfer from energetic ion to electron gas, a simple, well-understood relationship can be assumed between the energy of the incident ion beam and the electronic stopping power of most materials [18]. Nuclear stopping refers to the elastic collisions between the projectile ion and nuclei of the target atoms.

For very light ions slowing down in heavy materials the nuclear stopping power is weaker than the electronic stopping power at all energies. A high-energy projectile ion that has just entered the material is slowed down by electronic stopping at first and moves almost in a straight path. When the ion has slowed down sufficiently, the collisions with nuclei becomes more probable, finally dominating the slowing down process. Now the projectile ions have a probability to be backscattered by the ion species constituting the sample. Each elastic scattering incident is treated as a Coulomb repulsion between the helium ion and the target nucleus. A theoretical treatment of the backscattering problem for an incident particle of mass m_{He} and target particle of mass m_{target} results in Equation 2.2, which indicates that the ratio of particle energies after collision E_1 and before collision E_0 depends on the masses of the incident particle and target particle and the scattering angle θ [18]; see Fig. 4.

$$\frac{E_1}{E_0} = \left[\frac{\left(m_{\text{target}}^2 - m_{\text{He}}^2 \sin^2\theta\right)^{1/2} + m_{\text{He}}\cos\theta}{m_{\text{target}} + m_{\text{He}}}\right]^2 \tag{2.2}$$

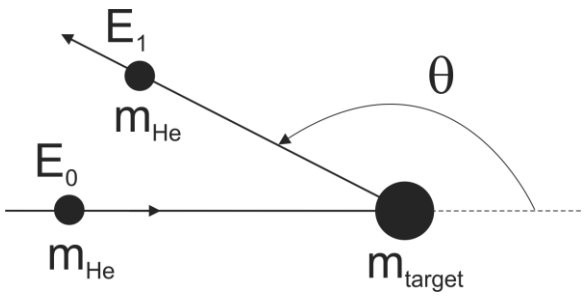

Figure 4. Energy is lost by an accelerated particle of mass m_{He} during large angle scattering by a stationary target particle of mass m_{target}. E_0 and E_1 are the kinetic energy of the accelerated particle before and after the backscattering and θ is the backscattering angle.

When multiple atomic species are present in the sample, the energy ratio E_0/E_1 is most sensitive to changes in the target atom mass when the backscattering angle between the incident ion and the backscattered ion θ is 180°, making this the ideal scattering angle. Due to the size of the detector, a backscattering angle of 170° is typically used [18].

The atomic species that are present in the sample can be identified using the energy loss of particles that are elastically backscattered from the atoms in the sample. Scattering cross section is a parameter that relates the distance of closest approach between the projectile and the target nucleus before the scattering and the angular distribution of the projectile after scattering and has the dimensions of an area. Equation

2.3 provides the expression for the scattering cross-section $\sigma(\theta)$ for each unique combination of incident and target nuclei, where Z_1 and Z_2 are the atomic numbers of the helium ion and the target atom respectively, e is the electronic charge, E is the incident kinetic energy, and θ is the scattering angle. To account for electronic stopping effects, the scattering cross-section is multiplied by the factor $F = (1 - 0.049Z_1Z_2^{4/3}/E)$ to give Equation 2.3.

$$\sigma(\theta) = F\left(\frac{Z_1 Z_2 e^2}{4E}\right)^2 \frac{1}{\sin^4 \theta/2} \tag{2.3}$$

Equation 2.4 relates the backscattered yield Y to the number of target atoms in the sample in atoms/cm^2 N_s and the total number of incident particles Q for a 100% efficient detector subtending a solid angle Ω, and for the geometry shown in Fig. 5 [17].

$$Y = \sigma(\theta)\Omega Q N_s \tag{2.4}$$

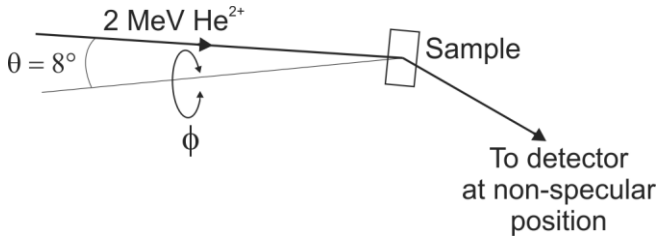

Figure 5. Sample schematic for random Rutherford backscattering spectrometry measurements. θ is the incident angle of the ion beam with respect to sample normal, and ϕ denotes azimuthal rotation.

The detector used for measuring the backscattered ion energy is a passivated implanted planar silicon detector. The detector operates by collecting the electron-hole pairs created by the incident particle in the depletion region of a Schottky barrier diode that is maintained at reverse-bias with an Au surface layer. Voltage pulses that are proportional to the backscattered particle energies E_1 are generated by the detector and amplified. Particles having energies in the same ranges are collected in the voltage bins or channels of a multichannel analyzer.

Random RBS measurements do not require any elaborate sample preparation, are not influenced by chemical bonding states, may impact the crystal coherence slightly, and provide quantitative compositional information for a sample without needing any reference standards. One shortcoming of random RBS is that the beam spot size is on the order of a few mm^2, which is considerably larger than that for other characterization techniques such as Secondary Ion Mass Spectrometry.

Simulated backscattering ion yield is obtained for the nominal cross-section for Sample a using a simulation package called RUMP [19] and is shown in Fig 6 as a solid purple curve. Also shown in the figure are simulations of backscattering signals arising from each element present in the layers of the structure, namely Bi (solid red), In (solid blue), As (solid dark green), Sb (solid light green), and Ga (solid orange), which combine to produce the overall simulated profile. Although the In, As, and Bi signals arise from the same InAsBi layer, the backscattered ion yield for these increasingly heavier elements arise at progressively larger backscattered ion energy ranges. Thus random RBS is well

suited for determining the concentration of heavy atoms present in a matrix of lighter atoms.

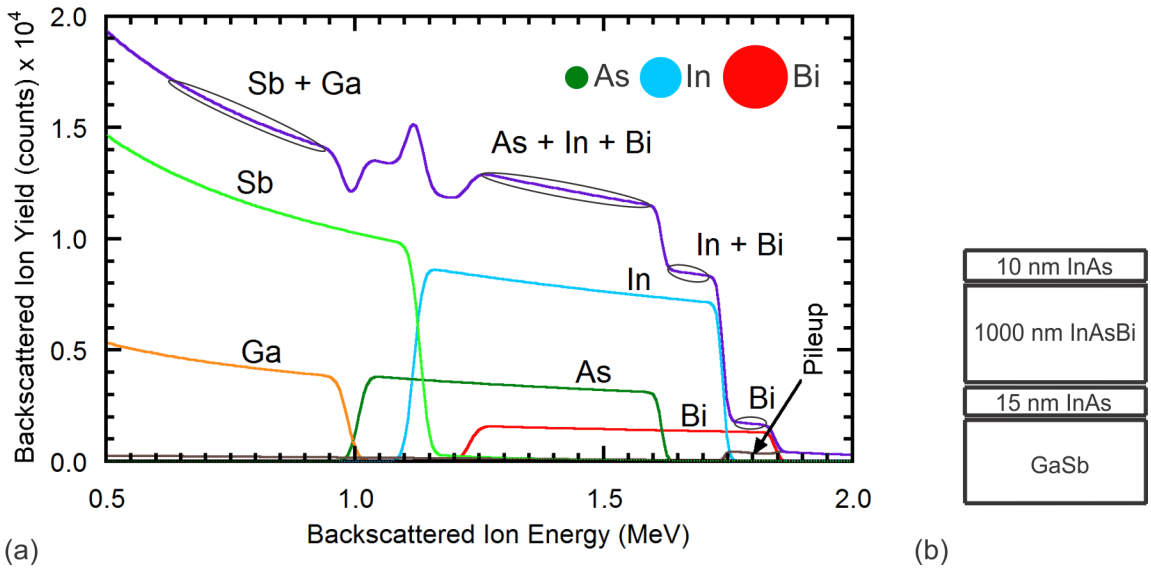

Figure 6. Simulated backscattered ion yield from bulk $InAs_{0.935}Bi_{0.065}$ on GaSb (Sample a), specified by the solid purple curve, and a breakdown of the simulation into backscattering signals arising from each element, namely Bi (solid red), In (solid blue), As (solid dark green), Sb (solid light green), and Ga (solid orange) in (a). The three solid circles shown above the simulation curves depict the relative atomic sizes of As, In, and Bi. The regions of the complete simulation curve arising due to backscattering from Bi, In + Bi, from As + In + Bi, and from Sb + Ga are marked by ellipses. The simulation cross-section is shown in (b)

Random RBS and ion channeling measurements are performed using 2.0 MeV doubly-ionized He atoms (He^{2+}) accelerated by a 1.7 MV General Ionex Tandetron accelerator and measured using a detector placed at a backscattering angle of 170°. The sample is mounted on a two-axis goniometer that enables polar and azimuthal rotations, in a vacuum chamber at a pressure of 10^{-6} Torr. During the random RBS measurements,

the ion beam is incident on the sample 8° from the normal while the sample is constantly rocked about the normal through an angular range of 5° at a rate of about one round cycle every two hours.

The random Rutherford backscattering ion yield from Sample a (solid red curve) is plotted as a function of the backscattered ion energy in Fig. 7. The sample cross section is shown in the inset. The backscattered ion yield is simulated with the InAsBi layer thickness and mole fraction as fitting parameters. The simulated ion yields for each element are shown as solid black curves; combined, these curves produce the overall simulated profile (solid blue curve) that closely matches the experimental curve (solid red curve). There exists a range of energies in the backscattered ion yield spectrum that is uniquely characteristic of Bi (1.765 to 1.858 MeV); as such the Bi mole fraction is determined to a high degree of accuracy with an uncertainty of ±0.0005. The Bi mole fraction for each sample is determined by fitting the height of the Bi signal, which expectedly increases with increasing Bi mole fraction as shown in Fig. 8a. The three regions of positive slope observed in the experimental curve identify the onsets of the In, As, and Bi signals at the lower InAs/InAsBi interface. The thickness of the InAsBi layer is determined by the horizontal positions of the peak and valley features in the spectrum between 0.9 and 1.3 MeV; increasing (decreasing) the InAsBi layer thickness shifts these features to the left (right); see Fig. 8b. The Bi mole fraction and InAsBi layer thickness determined from the RBS measurements and analysis are shown in Table II.

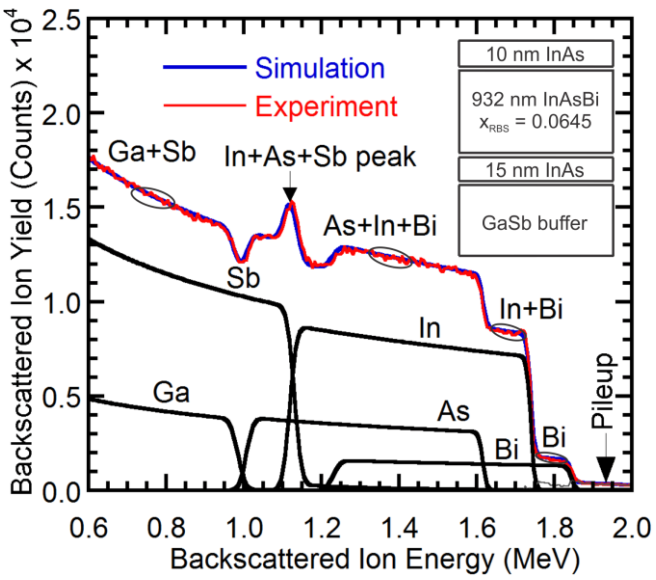

Figure 7. Random Rutherford backscattering spectrometry ion yield from bulk $InAs_{0.935}Bi_{0.065}$ on GaSb (Sample a) as a function of the backscattered ion energy. The sample cross-section is given in the inset. The solid red curve is the experimental result for Sample a whose structure is given in the figure inset. The solid black curves are the simulated backscattered ion yields from each elemental constituent of each layer in the structure, the sum of which forms the solid blue curve, which is the complete simulation profile. Interference of signals from nearly simultaneous arrivals of backscattered ions at the detector produces the pileup tail above 1.86 MeV in the experimental data.

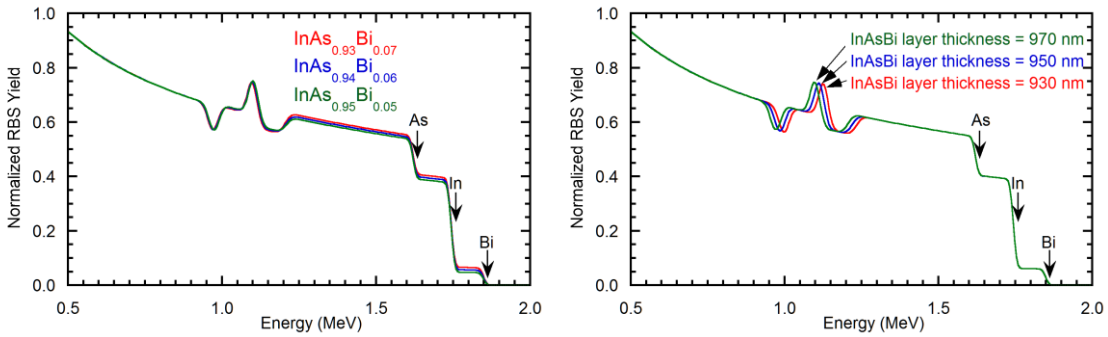

Figure 8. Simulated backscattered ion yield from bulk InAsBi on GaSb (a) as a function of bismuth mole fraction and (b) as a function of InAsBi layer thickness.

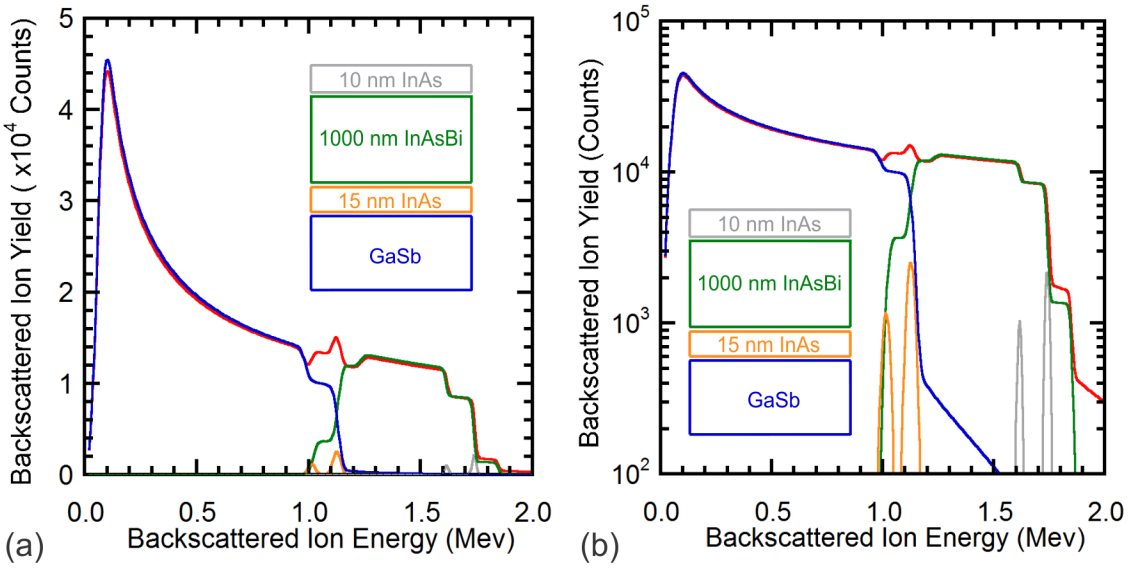

Figure 9. Simulated backscattered ion yield from bulk $InAs_{0.935}Bi_{0.065}$ on GaSb (Sample a) shown as the solid red curve, and breakdown of the complete simulation profile into backscattering signals from the individual layers in the sample in (a) for linear and (b) for exponential scales. The simulated cross-section is shown as insets.

Table II: Structural properties of bulk InAsBi layers grown on GaSb. Random Rutherford backscattering spectrometry measurements provide the Bi mole fraction x_{RBS} and layer thickness of the InAsBi layer. X-ray diffraction measurements provide the tetragonal distortion and lattice constant for the main diffraction peak $\varepsilon_\perp(1)$ and a_1 and the average diffraction $\overline{\varepsilon_\perp}$ and $\overline{a_x}$.

Sample	Bi mole fraction x_{RBS}	InAsBi layer thickness (nm)	Tetragonal distortion (ppm)		Lattice constant (Å)	
			$\varepsilon_\perp(1)$	$\overline{\varepsilon_\perp}$	a_1	$\overline{a_x}$
a	0.0645	932	-496	-720	6.0941	6.0935
b	0.0620	918	-965	-1082	6.0928	6.0924
c	0.0595	983	-1531	-1625	6.0911	6.0908
d	0.0558	927	-1969	-2103	6.0898	6.0894
e	0.0573	938	-2050	-2168	6.0896	6.0892
f	0.0530	944	-2536	-2664	6.0882	6.0878
g	0.0503	927	-3000	-3092	6.0868	6.0865

2.3. X-Ray Diffraction

X-ray diffraction (XRD) is a widely used technique for characterizing the structure of epitaxial films. It gives a measure of the long-range order, from which the epilayer properties such as strain, thickness, and film composition can be determined.

The wavelength of X-rays is on the order of the interatomic distance in a typical crystal, making X-rays ideal for the study of diffraction from crystalline materials. Diffraction occurs when atoms in a periodic lattice scatter radiation coherently, producing constructive interference at specific angles. The diffraction from different planes of atoms produces a diffraction pattern containing information about the planar arrangement of the atoms. An epitaxial layer produces strong diffraction peaks called Bragg diffraction peaks. Sometimes, there is interaction between the diffracted waves from the substrate and from the film layers, producing additional peaks that will contain microstructural information.

During XRD measurements, the X-ray wavelength λ is fixed, the incident angle θ is varied, and the plane normal is ensured to be parallel to the vector bisecting the angle between the incident beam and the diffracted beam. For atoms arranged in parallel planes having equal spacing d_{hkl}, constructive interference occurs when Bragg's law

$$n\lambda = 2d_{hkl}\sin\theta \tag{2.5}$$

is satisfied [20]; n is the order of reflection and is a positive integer. A family of planes will produce a diffraction peak only at a particular incident angle, and the peak positions are determined by the spacing between the diffraction planes.

Reciprocal space maps of the studied samples shown in Fig. 10 are performed in the vicinity of the (115)-reflection of the GaSb substrate. The peak separation in the growth direction reciprocal lattice (vertical axis) increases with decreasing Bi mole fraction, indicating a steady increase in the layer tensile strain. For all samples, the GaSb and InAsBi diffraction peaks line up at the in-plane reciprocal lattice position 2.32 nm^{-1}, confirming that all of the samples are coherently strained.

High-resolution X-ray diffraction (XRD) measurements are obtained using a PANalytical X'Pert Pro materials research X-ray diffractometer and Cu $K\alpha_1$ radiation. The incident beam optics consist of an X-ray mirror and a 2-crystal Ge (220) 4-bounce monochromator with a 0.25° divergence slit, and a 1.65 mm width mask. The use of the narrow mask ensures that the sample area probed by X-ray is comparable to the sample area probed by RBS (1 mm × 2 mm). The diffracted beam optics consist of a triple axis monochromator with a 0.50° slit placed before the detector.

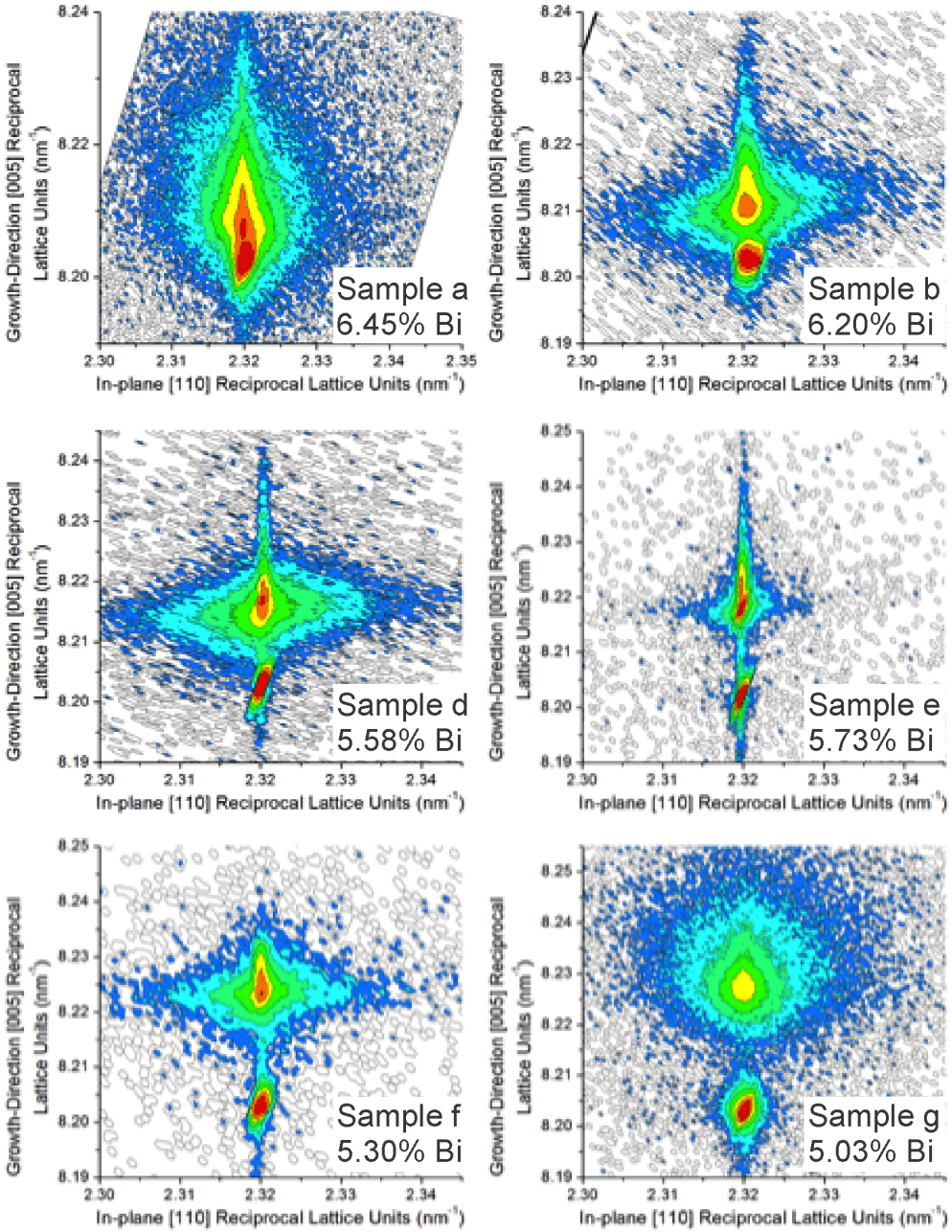

Figure 10. Reciprocal space maps of InAsBi on GaSb (Samples a, b, c, d, f, and g) in the vicinity of (115) reflection.

The symmetric (004) coupled ω-2θ XRD patterns are measured at a random azimuthal angle, arbitrarily assigned $\phi = 0°$, after which the sample is rotated through an azimuthal angle of 180° and a second XRD pattern is measured. By averaging the $\phi = 0°$ and $\phi = 180°$ XRD patterns (see Fig. 11 and Fig. 12), the effect of the wafer offcut on the peak separation is minimized to 0.0001° for offcut angles up to ±0.1° which is the offcut tolerance supplied by the wafer manufacturer [11,12]. The solid black curve in Fig. 11a shows the averaged ω-2θ XRD pattern for Sample a plotted as a function of diffraction angle on the upper horizontal-axis and angle relative to the substrate diffraction peak on the lower horizontal-axis. Moving from left to right there is a sharp peak from the GaSb substrate at $\theta - \theta_{sub} = 0.0000°$ and a sharp peak from the 932 nm thick InAsBi layer at $\theta - \theta_{sub} = 0.0167°$. Further to the right of the main InAsBi peak, there is a broad sideband peak in the range $0.0350° < \theta - \theta_{sub} < 0.1050°$.

The presence of this sideband peak is consistent with the lateral variation of bismuth mole fraction observed in the bright field cross-sectional transmission electron micrographs of this sample [7,21], as the reduced diffraction intensity and increased broadness at larger diffraction angles indicate that the lower mole fraction region constitutes a significantly smaller volume of InAsBi than the higher mole fraction region that forms the main peak. The bright field cross-sectional transmission electron micrograph of Sample a, shown in Fig. 11b, indicates that the material exhibits excellent crystallinity, no ordering, no visible defects over large lateral distances, and lateral fluctuations of the Bi mole fraction on a 10 nm length scale [21].

Similar broad diffraction features are found in the diffraction spectra of all the other samples shown in Fig 12. Also, decreasing the net Bi content of the epilayer expectedly shifts the InAsBi diffraction signal to higher diffraction angles due to the smaller lattice constant and greater tetragonal distortion in the layer. The XRD patterns discussed here are obtained before the samples are probed using random RBS or ion channeling. A broadening of the XRD peaks is observed after the sample is probed using either of these techniques, indicating that the coherence of the crystal lattice is slightly modified.

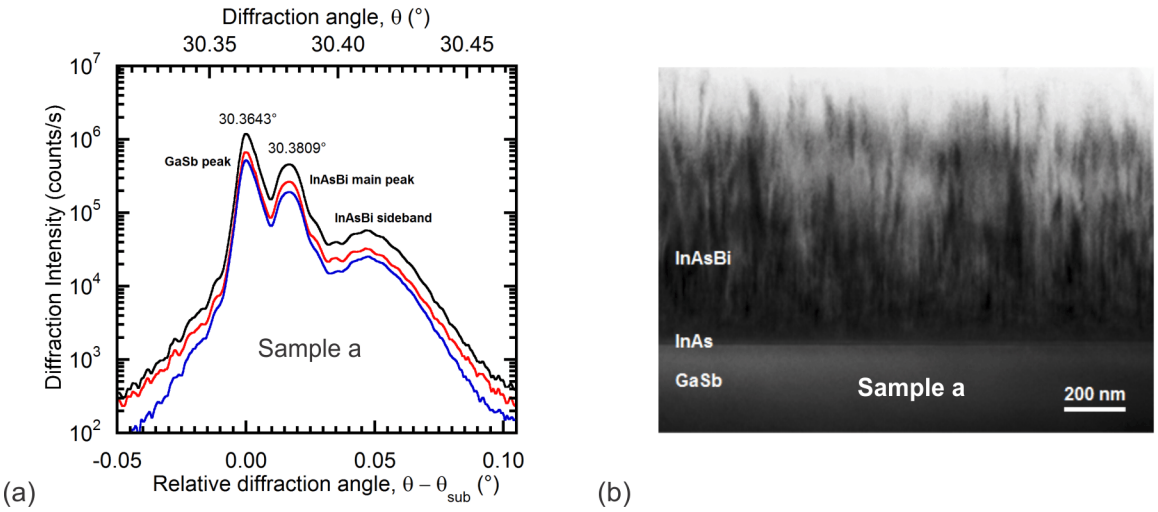

Figure 11. (a) Coupled ω-2θ X-ray diffraction pattern from the (004) planes of bulk $InAs_{0.935}Bi_{0.065}$ on GaSb (Sample a) shown as the solid black curve, which is an average of measurements taken at azimuthal angles 0° (solid red curve) and 180° (solid blue curve). (b) Bright field cross-sectional transmission electron micrograph of InAsBi on GaSb (Sample a) showing lateral compositional modulation of bismuth content. *Transmission Electron Micrograph acquired by Jing Lu and Dr. David J. Smith at Arizona State University* [13].

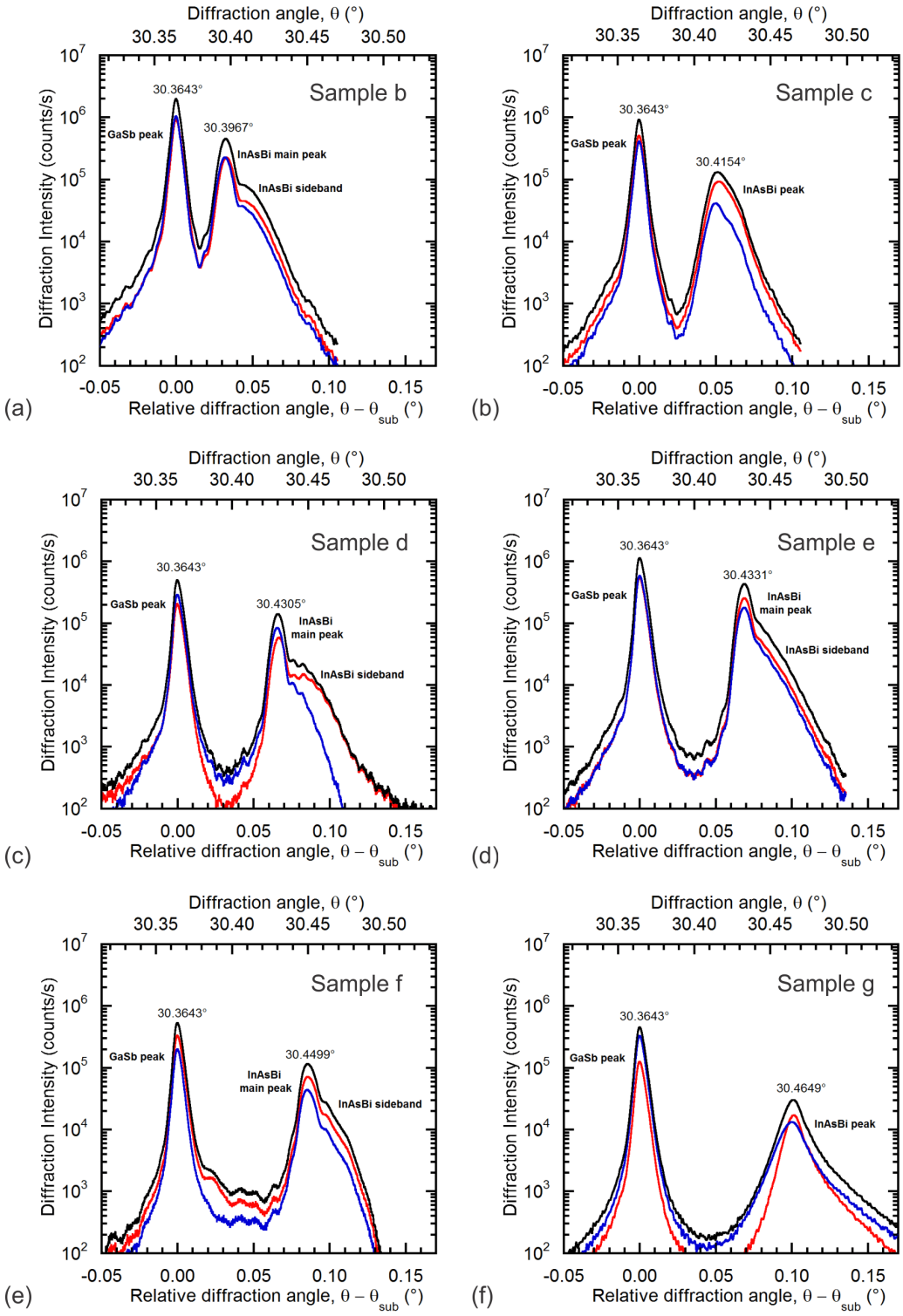

Figure 12. Coupled ω-2θ X-ray diffraction pattern from the (004) planes of bulk InAsBi on GaSb (samples b through g).

The X-ray diffraction pattern including the diffraction sideband is modeled using simulated diffraction peaks. The commercial PANalytical X'Pert Epitaxy dynamical X-ray diffraction software [22] is used to obtain the shapes of diffraction from GaSb (see Fig. 13a) and 932 nm thick InAsBi layers containing varying amounts of Bi (see Fig. 13b).

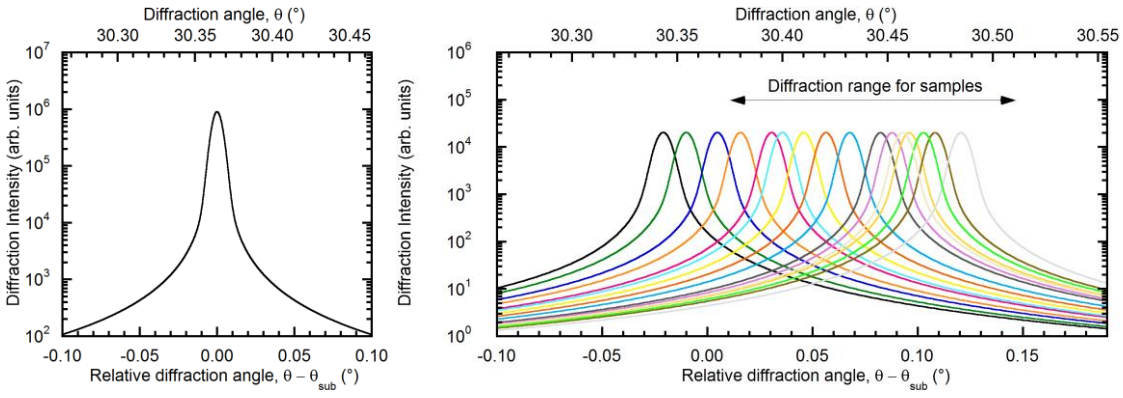

Figure 13. (a) Simulation of X-ray diffraction signal from GaSb and (b) 932 nm thick InAsBi layers containing varying amounts of bismuth.

The GaSb and InAsBi simulated diffraction peaks are parameterized by the Gaussian-Lorentzian peak model [23] given in Equations 2.6 and 2.7.

$$I(\theta) = I_p\left(A_G\frac{\sqrt{\ln 2}}{\Gamma_G\sqrt{\pi}}e^{\frac{-ln2(\theta-\theta_{sub})^2}{{\Gamma_G}^2}} + (1-A_G)\frac{\Gamma_L}{\pi}\frac{1}{(\theta-\theta_{sub})^2+{\Gamma_L}^2}\right) \tag{2.6}$$

$$I(\theta) = I_p\left(A_G\frac{\sqrt{\ln 2}}{\Gamma_G\sqrt{\pi}}e^{\frac{-ln2((\theta-\theta_{sub})-\theta_i)^2}{{\Gamma_G}^2}} + (1-A_G)\frac{\Gamma_L}{\pi}\frac{1}{((\theta-\theta_{sub})-\theta_i)^2+{\Gamma_L}^2}\right) \tag{2.7}$$

where I_p is the peak intensity, A_G is the Gaussian content of the curve, $A_L = 1 - A_G$ is the Lorentzian content of the curve, $2\Gamma_G$ is the Gaussian full width at half maximum, $2\Gamma_L$ is the Lorentzian full width at half maximum, $\theta - \theta_{sub}$ is the diffraction angle relative to the substrate peak position The Gaussian-Lorentzian model for the GaSb substrate peak centered at $\theta_{sub} = \theta_{GaSb} = 30.364289°$ is given by Equation 2.6 (see Fig 14a) and the InAsBi layer peaks centered at θ_i is given by Equation 2.7 (see Fig 14b).

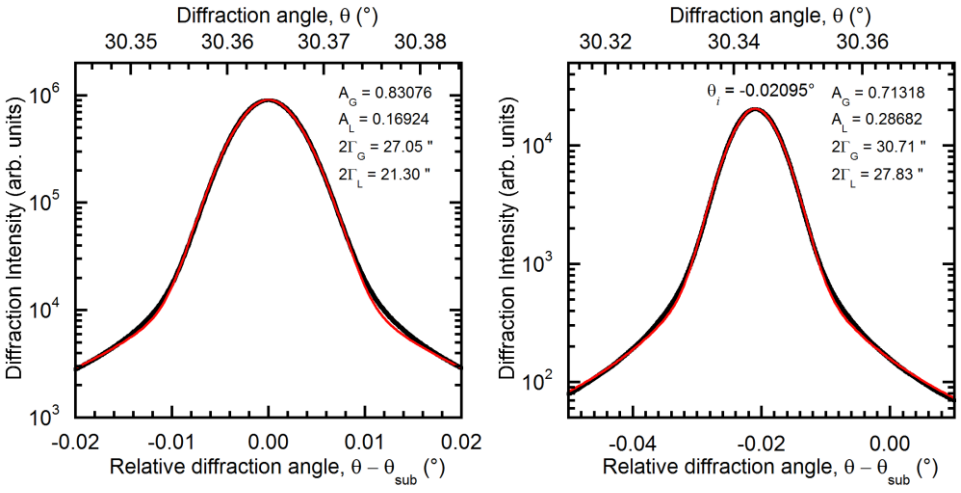

Figure 14. Simulation of X-ray diffraction signal from (a) GaSb substrate and (b) InAsBi epilayer shown as solid black curves, and fits to the simulations using Equations 2.6 and 2.7, shown as solid red curves. The Gaussian character, Lorentzian character, and the full widths at half maximum of the Gaussian component and Lorentzian component of each fits are summarized in the figures.

The Gaussian-Lorentzian model parameter values for the simulated diffraction peaks are summarized in Table III. There is one set of parameters for the substrate peak and another set of parameters as a function of diffraction angle θ_i for the InAsBi layer diffraction peaks. The parameter values are determined by a least squares fit of the Gaussian-Lorentzian model to the simulated diffraction peaks. During the fitting process, the uncertainty in the simulated peak intensities are assumed to be proportional to the square root of the simulated counts, which for example is an uncertainty of 1 for 1 count/s, 10 for 10^2 counts/s, and 100 for 10^4 counts/s. This enables the model to fairly characterize the tail as well as the peak and is a realistic uncertainty for this type of measurement where the signal ranges over orders of magnitude. Other possibilities would be an uncertainty proportional to intensity that would favorably fit the tail or a constant uncertainty that would favorably fit the peak, which is the default when uncertainty analysis is ignored altogether. Fig. 15 shows the InAsBi model parameters as functions of diffraction angle.

Table III: Best-fit Gaussian-Lorentzian model parameters for simulated diffraction from GaSb and InAsBi.

Material	Model Parameters
GaSb	$\theta_{sub} = 30.364289° \ (fixed)$ $A_G = 0.83076$ $A_L = 0.16924$ $2\Gamma_G = 0.007513°$ $2\Gamma_L = 0.005916°$
InAsBi	$\theta_i \ (i = 1,2,3,\ldots,m)$ $A_G(\theta_i) = 0.71324 + 0.00261\ \theta_i°$ $A_L(\theta_i) = 0.28676 - 0.00261\ \theta_i°$ $2\Gamma_G(\theta_i) = 0.008529° - 0.000020\ \theta_i°$ $2\Gamma_L(\theta_i) = 0.007732° - 0.000012\ \theta_i°$

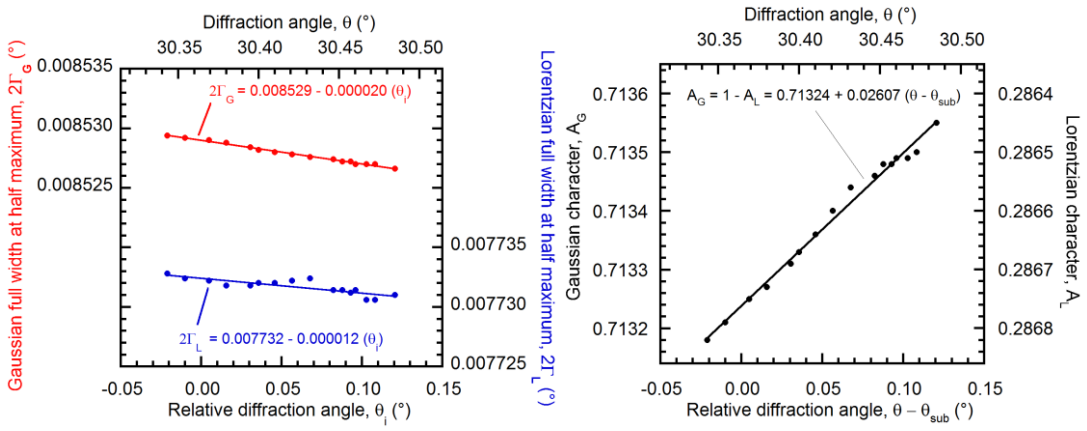

Figure 15: (a) Full widths at half maximum of the Gaussian (left-hand vertical-axis) and Lorentzian (right-hand vertical-axis) components and (b) Gaussian character (left-hand vertical-axis) and Lorentzian character (right-hand vertical-axis) of InAsBi Gaussian-Lorentzian as functions of peak diffraction angle (upper horizontal-axis) and peak angle relative to GaSb diffraction peak (lower horizontal-axis).

The complete model of the diffraction pattern is sum of Gaussian-Lorentzian peaks consisting of a GaSb peak, an InAsBi main peak (i = 1), and several InAsBi sideband peaks (i = 2, 3, 4, ..., m):

$$\text{Model} = I_p(\theta_{sub}) \times \begin{pmatrix} A_G \dfrac{\sqrt{\ln 2}}{\Gamma_G\sqrt{\pi}} e^{\frac{-ln2\,(\theta-\theta_{sub})^2}{{\Gamma_G}^2}} \\ +A_L \dfrac{\Gamma_L}{\pi} \dfrac{1}{(\theta-\theta_{sub})^2 + {\Gamma_L}^2} \end{pmatrix}$$

$$+\sum_i I_p(\theta_i) \times \begin{pmatrix} A_G(\theta_i) \dfrac{\sqrt{ln\,2}}{\Gamma_G(\theta_i)\sqrt{\pi}} e^{\frac{-ln2\left((\theta-\theta_{sub})-\theta_i\right)^2}{\Gamma_G(\theta_i)^2}} \\ +A_L(\theta_i) \dfrac{\Gamma_L(\theta_i)}{\pi} \dfrac{1}{((\theta-\theta_{sub})-\theta_i)^2 + \Gamma_L(\theta_i)^2} \end{pmatrix} \tag{2.8}$$

where θ_i is the position and $I_p(\theta_i)$ is the intensity of each peak, and m is the number of peaks fit to the InAsBi layer main peak and sideband.

The model in Equation 2.8 is fit to the diffraction pattern from all the studied samples in Fig. 16 and Fig. 17 and is displayed as a solid orange curve overlaying the solid black experimental curve. Also shown is the breakdown of the model into individual peaks for the substrate and 9 constituent InAsBi peaks (solid red curves). The model parameter values for Sample a are summarized in Table IV.

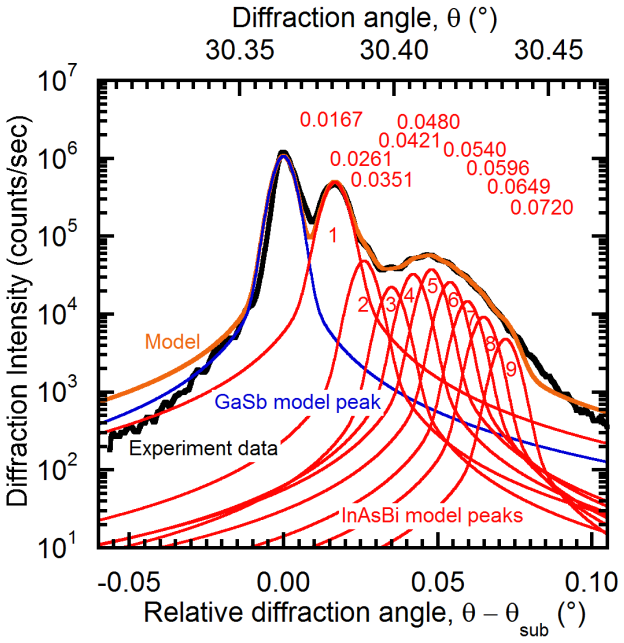

Figure 16. X-ray diffraction measurement of InAsBi on GaSb (sample a) (solid black curve), model fit to the experiment data (solid orange curve), GaSb model peak (solid blue curve), and InAsBi model peaks (solid red curves). The InAsBi model peaks are numbered 1 through 9 and are marked by their peak angles.

The out-of-plane (growth direction) tetragonal distortion $\varepsilon_\perp$ is determined from the substrate-layer peak separation in the coupled (004) X-ray diffraction pattern. The tetragonal distortion values for the tensilely strained InAsBi layers are summarized in Table II as $\varepsilon_\perp(1)$ for that given by the position of the main InAsBi diffraction peak (1 in Fig. 16) and as $\overline{\varepsilon_\perp}$ for that given by the integrated-intensity-weighted average of all InAsBi diffraction peaks (1 through 9 in Fig. 16) that includes the smaller but significant contribution of the sideband diffraction to the overall average tensile strain in the InAsBi layer. The bulk InAsBi lattice constants inferred from the tetragonal distortion are as well provided in Table II, where a_1 is inferred from the main peak and $\overline{a_x}$ is inferred from the average tetragonal distortion.

Table IV: Model parameter values for the sum of Gaussian-Lorentzian peaks model (Equation 2.8) fit to the experimental X-ray data from Sample a and shown in Fig. 16. Each peak position θ_i is specified in degrees and the integrated intensity for each peak $I_p(\theta_i)$ is specified in counts/s.

Model peak type	i	θ_i (°)	$I_p(\theta_i)$ (counts/s)
GaSb substrate	-	0	8750
InAsBi layer	1, main peak	0.01666	4850
	2	0.02612	474
	3	0.03505	218
	4	0.04206	320
	5	0.04800	367
	6	0.05403	253
	7	0.05962	143
	8	0.06491	90
	9	0.07200	47

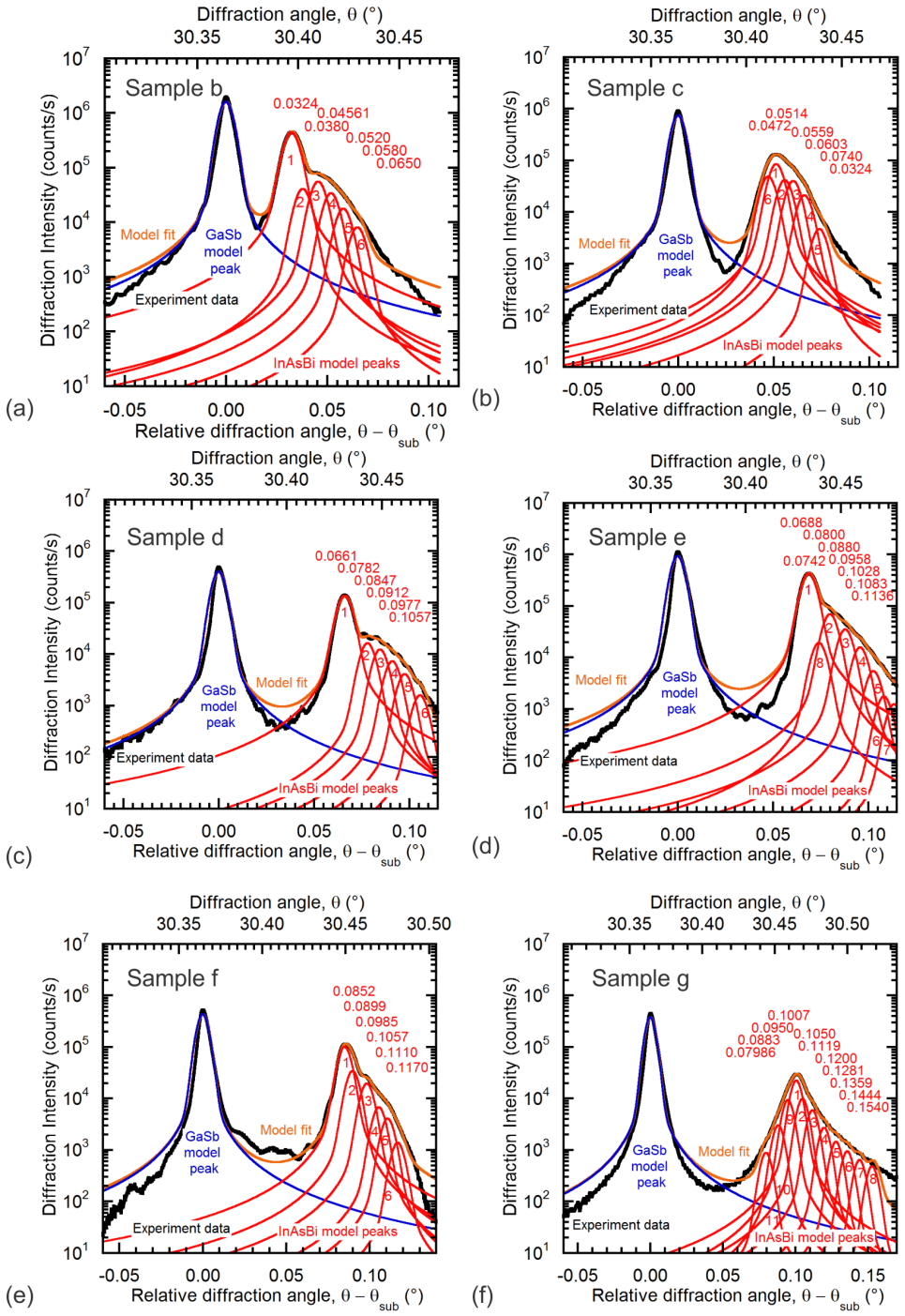

Figure 17. X-ray diffraction measurement of InAsBi on GaSb (samples b through g) (solid black curve), model fit to the experiment data (solid orange curve), GaSb model peak (solid blue curve), and InAsBi model peaks (solid red curves). The InAsBi model peaks are marked by their peak angles.

When the strain and hence the substrate-layer angular separation is small the out-of-plane tetragonal distortion is accurately described to first order by [24]

$$\varepsilon_{\perp}(i) = -\frac{\theta_{layer} - \theta_{sub}}{\tan(\theta_{sub})} = -\frac{\theta_i}{\tan(\theta_{sub})} \quad , \tag{2.9}$$

where θ_{sub} is the substrate diffraction peak position, θ_{layer} is the layer diffraction peak position, and $\theta_i = \theta_{layer} - \theta_{sub}$ is the layer diffraction peak position relative to the substrate diffraction peak position. The out-of-plane tetragonal distortion determined from the InAsBi main diffraction peak (i = 1) is given by

$$\varepsilon_{\perp}(1) = -\frac{\theta_1}{\tan(\theta_{sub})} \tag{2.10a}$$

and the average out-of-plane tetragonal distortion is given by

$$\overline{\varepsilon_{\perp}} = \frac{\sum_i [\varepsilon_{\perp}(i) \times I_p(i)]}{\sum_i I_p(i)} \tag{2.10b}$$

which is an $I_p(\theta_i)$ intensity weighted average over all simulated InAsBi peaks. The results are compared in Table II where the average tetragonal distortion values $\overline{\varepsilon_{\perp}}$ are consistently larger than those determined using the main peak only $\varepsilon_{\perp}(1)$ as the diffraction sideband arises from small regions of lower Bi mole fraction.

To calculate the lattice constant of free-standing material from the tetragonal distortion of strained material, it is necessary to know Poisson's ratio which quantifies the out-of-plane compression that results from the in-plane biaxial tension. For ternary alloys, material parameters such as Poisson's ratio are typically linearly interpolated as a function of mole fraction between the respective values for the constituent binaries.

However, since Poisson's ratio for InBi has not been measured or calculated it is estimated as follows.

The elastic constants (C_{11} and C_{12}) for zinc blende InP, InAs, and InSb are well known [16] and are compared as a function of group-V atomic number (Z) in Fig. 18; see solid circles and left-hand vertical axis. Power law equations are fit to the results and shown by solid blue and red curves along with the best fit parameters in equation form. The C_{11} and C_{12} values for InBi are estimated by using the power law fit out to the atomic number for Bi (Z = 83), which results in C_{11} = 60.31 GPa and C_{12} = 32.52 GPa. Poisson's ratio is related to the elastic constants by the Equation 2.11, which produces a value of 0.3505 for InBi. Poisson's ratios for InP, InAs, InSb, and InBi is plotted with solid squares on the right-hand vertical axis of Fig. 18; and does not show a clear trend.

$$\nu = \frac{C_{11}}{C_{11} + C_{12}} \tag{2.11}$$

For comparison Poisson's ratio for each binary is plotted on right-hand vertical axis of Fig. 18; and does not show such a clear trend as the elastic constants.

Assuming that Poisson's ratio for the InAsBi ternary ν_x varies linearly with Bi mole fraction, x_{RBS}, then Poisson's ratio for InAsBi can be expressed as

$$\nu_x = \nu_{InAs} + (\nu_{InBi} - \nu_{InAs})x_{RBS} \ , \tag{2.12}$$

where ν_{InAs} = 0.3521 [16] and ν_{InBi} = 0.3503 are Poisson's ratio for InAs and InBi. Using these values, Poisson's ratio only varies slightly in the fifth significant figure (from 0.35198 to 0.35201) over the range of Bi mole fractions examined in this work.

Therefore, a constant Poisson's ratio of ν_{InAsBi} = 0.3520 near that of InAs, is utilized in the analysis of the InAsBi samples presented here.

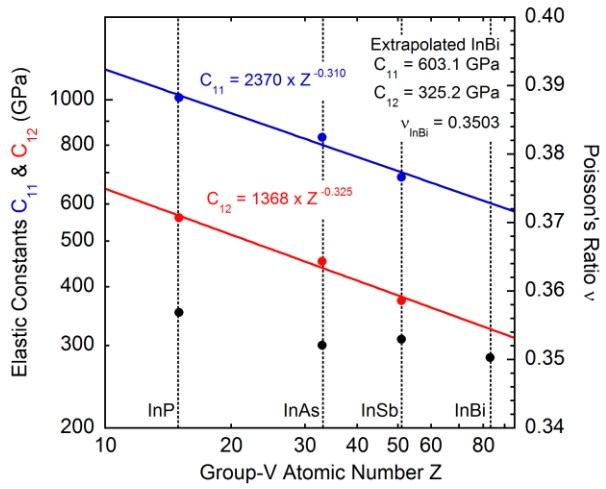

Figure 18. For Indium-containing III-V binary semiconductors, the elastic constants C_{11} and C_{12} (solid black circles, left-hand vertical-axis) and Poisson's ratio (solid black squares, right-hand vertical-axis) are plotted as functions of group-V atomic number Z (horizontal axis). Power law fits to the elastic constants are shown as solid black curves with the best fit equations indicated. Poisson's ratio for InBi (Z = 83) is estimated from the extrapolated values of C_{11} and C_{12}.

Two sets of InAsBi lattice constants are determined and summarized in Table II: one using Equation 2.13a and the out-of-plane tetragonal distortion $\varepsilon_{\perp}(1)$ given by the main InAsBi diffraction peak and one using Equation 2.13b and the average out-of-plane tetragonal distortion $\overline{\varepsilon_{\perp}}$; where a_{GaSb} = 6.09557 Å [16] is the GaSb lattice constant.

$$a_1 = \left[\left(\frac{1-\nu_{InAsBi}}{1+\nu_{InAsBi}}\right)\varepsilon_{\perp}(1)+1\right]a_{GaSb} \qquad (2.13a)$$

$$\overline{a_x} = \left[\left(\frac{1-\nu_{InAsBi}}{1+\nu_{InAsBi}}\right)\overline{\varepsilon_\perp} + 1\right] a_{GaSb} \tag{2.13b}$$

The InAsBi lattice constants determined by XRD are plotted as a function of the Bi mole fraction measured by RBS and are shown in Fig. 19. The open circles are the lattice constants associated with the main diffraction peak (a_1) and the solid circles are those given by the average diffraction intensity ($\overline{a_x}$). The following linear equation is fit to the data with one end fixed at the well-known InAs lattice constant a_{InAs} = 6.05816 Å [16] and the other end is the best fit estimate of the lesser known InBi lattice constant a_{InBi}.

$$a_{InAsBi} = a_{InAs} + (a_{InBi} - a_{InAs})x \tag{2.14}$$

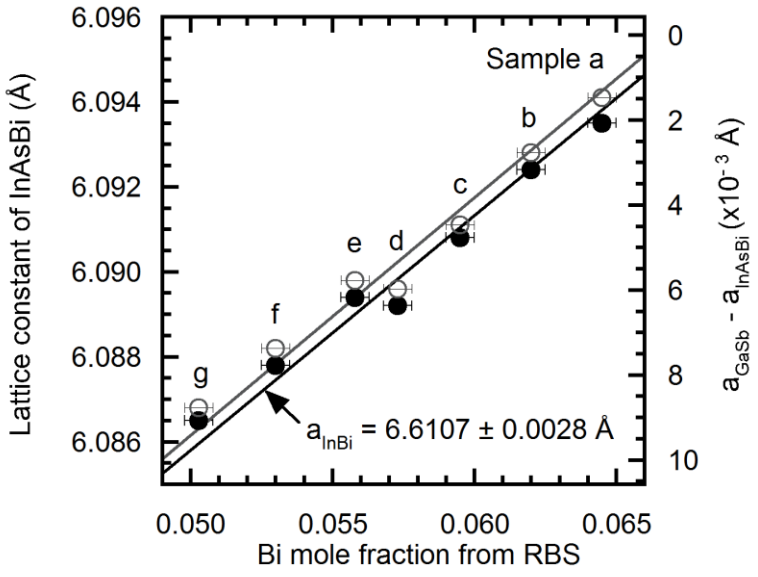

Figure 19. Unstrained bulk InAsBi lattice constant (left-hand vertical-axis) as a function of the Bi mole fraction determined by Rutherford backscattering for samples a through g.

The difference in the lattice constant relative to GaSb is shown on the right-hand vertical-axis. The open circles show the lattice constant specified by the main diffraction peak and the solid circles show the average lattice constant determined by analysis of the main and the sideband diffraction peaks. The solid lines are linear fits to the data. The best-fit InBi lattice constant for the average lattice constant dataset is shown.

Since the RBS measurements provide the average mole fraction of the InAsBi layer, the InBi lattice constant is more accurately determined using the average lattice constants of the InAsBi layers (solid circles) with the best fit value of a_{InBi} = 6.6107±0.0028 Å. When fitting to the InAsBi lattice constants provided by the main diffraction peak (open circles) the best fit value is larger at 6.6177±0.0028 Å, which overestimates the value by about 0.1%. The difference between the two values (0.0070 Å) is larger than the uncertainty (0.0028 Å), indicating that the small regions of lower mole fraction significantly contribute to the average lattice constant and need to be considered.

Values for the InBi lattice constant have previously been determined through the analysis of the mole fraction and the lattice constant of InSbBi [10,15], InAsBi [11,12], and InPBi [13,14], or from theoretical calculations [6]. Since the reported values of the InBi lattice constant span a significant range from 6.500 Å to 7.292 Å, accurate measurements of the lattice constant of zinc blende InBi are of great interest.

The InBi lattice constant values reported to date [6,10-15] are summarized in Fig. 20. The InBi lattice constant determined in this work is shown as a solid blue circle near the bottom-right corner of the figure. This value is in reasonable agreement with many of the previously reported values [10,12,14,15] where up to 3.3% Bi containing

samples were studied. The Bi content in the bulk InAsBi films studied in this work ranges from 5.03% to 6.45%, which is higher than the Bi content of the ternary materials studied in previous work, < 4.0% Bi [10-15]. Therefore, the InBi lattice constant reported here is expected to be more accurate. Two of the data points shown in the figure utilizes Energy Dispersive Spectroscopy (EDS) to measure the Bi mole fraction [10,11].

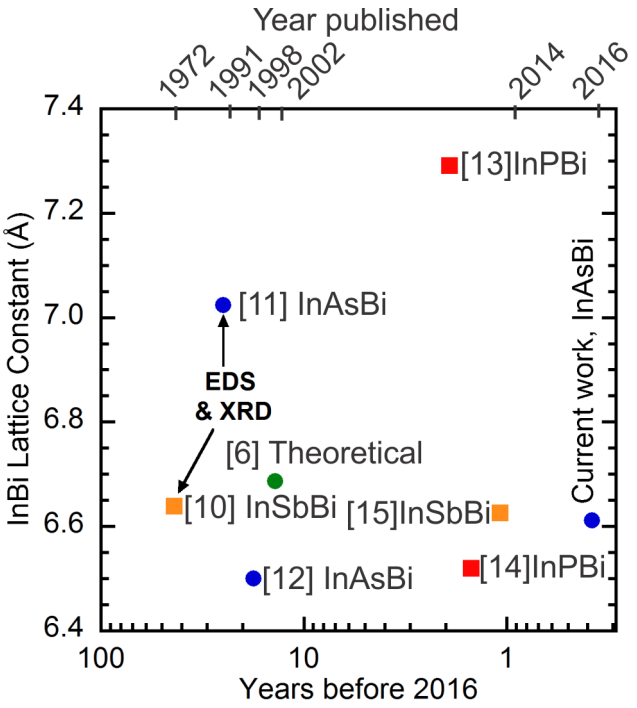

Figure 20. Reported InBi lattice constant versus year published (upper horizontal-axis) and years before 2016 (lower horizontal-axis). A theoretical value calculated using density functional theory [16] is indicated by a solid green circle. Experimentally determined values are labeled by reference number and material system studied with solid orange squares for InSbBi, solid blue circles for InAsBi, and solid red squares for InPBi. Rutherford backscattering spectrometry was used for all except for Ref. 10 and 11 indicated as "EDS & XRD" where energy dispersive spectroscopy was instead used to determine Bi mole fraction.

Using the lattice constant determined for InBi the X-ray diffraction measurements are further analyzed to study the mole fraction variation within each sample. Diffraction patterns of the studied samples indicate the segregation of InAsBi into a main volume at a single dominant composition and a smaller volume of a narrow range of lower InAsBi compositions, which is in agreement with the lateral compositional variation on the scale of several tens of nanometers observed in bright-field transmission electron micrographs of Samples a and g [7,21]. The fraction of InAsBi consisting of the dominant main composition and of those compositions indicated by the sideband diffraction are estimated from the various InAsBi diffraction peak intensities using the following equations for all the samples and summarized in Table V.

$$\text{Main InAsBi volume fraction} = \frac{I_p(1)}{\sum_i I_p(i)}\,, i\ =\ 1, 2, 3, \dots, \text{m} \tag{2.15a}$$

$$\text{Sideband InAsBi volume fraction} = \frac{\sum_j I_p(j)}{\sum_i I_p(i)}\,, i\ =\ 1, 2, 3, \dots, \text{m}, \quad j\ =\ 2, 3, 4\,, \dots, \text{m} \tag{2.15b}$$

The mole fraction of the dominant single composition region and the weighted average mole fraction of the lower composition region are determined using the following equations and summarized in Table V.

$$x_1 = \frac{a_1 - a_{InAs}}{a_{InBi} - a_{InAs}} \tag{2.16a}$$

$$\overline{x}_{sideband} = \frac{\left[\left(\frac{1-\nu_{InAsBi}}{1+\nu_{InAsBi}}\right)\frac{\sum_i[\varepsilon_\perp(i)\times I_p(i)]}{\sum_i I_p(i)} + 1\right] a_{GaSb} - a_{InAs}}{a_{InBi} - a_{InAs}}, \qquad (2.16b)$$

$$i = 2, 3, 4, \ldots, \mathrm{m}$$

where, a_1 is the lattice constant of the dominant single mole fraction region (see Equation 2.13a) and a_{InAs} = 6.05816 Å, a_{InBi} = 6.6107 ±0.0028 Å, and a_{GaSb} = 6.09557 Å are the InAs, InBi, and GaSb lattice constants; ν_{InAsBi} = 0.3520 is Poisson's ratio, $\varepsilon_\perp(i)$ is the out-of-plane tetragonal distortion (see Equation 2.9), and $I_p(i)$ is the integrated intensity of each simulated peak. Note that only the sideband peaks ($i = 2, 3, 4, \ldots, \mathrm{m}$) are considered in Equation 2.16b.

The average mole fraction determined solely from the XRD data is calculated using the following equation and is summarized and compared to that determined by RBS in Table V.

$$\overline{x}_{XRD} = \frac{\overline{a_x} - a_{InAs}}{a_{InBi} - a_{InAs}} \qquad (2.17)$$

where, $\overline{a_x}$ is the average InAsBi lattice constant (see Equation 2.10b). The uncertainty in $\overline{x}_{XRD}$ is the integrated-intensity-weighted average of the standard deviation of the mole fraction determined for all peaks ($x_1, x_2, x_3, \ldots, x_m$). The analysis shown in Table V indicates that approximately 70% of the InAsBi is alloyed as the main composition while the remaining 30% is alloyed as the narrow range of compositions corresponding to the diffraction sideband.

Table V: Lateral distribution of Bi mole fraction in InAsBi layers and comparison with average values.

Sample number	Average in-plane strain (%)	InAsBi region with single dominant mole fraction		InAsBi region with range of smaller mole fractions			Average Bi mole fraction from XRD, $\overline{x}_{XRD}$	Average Bi mole fraction from RBS, $\overline{x}_{RBS}$
		volume fraction	mole fraction, x_1	volume fraction	mole fraction range	average mole fraction, $\overline{x}_{sideband}$		
1	0.0345	0.72	0.0651	0.28	0.0587 - 0.0631	0.0609	0.0639 ± 0.0039	0.0645 ± 0.0005
2	0.0519	0.74	0.0626	0.26	0.0589 - 0.0615	0.0602	0.0620 ± 0.0023	0.0620 ± 0.0005
3	0.0779	0.65	0.0596	0.35	0.0576 - 0.0600	0.0588	0.0591 ± 0.0022	0.0595 ± 0.0005
4	0.1009	0.77	0.0573	0.23	0.0530 - 0.0556	0.0543	0.0566 ± 0.0030	0.0558 ± 0.0005
5	0.1040	0.74	0.0569	0.26	0.0530 - 0.0558	0.0544	0.0562 ± 0.0024	0.0573 ± 0.0005
6	0.1279	0.60	0.0543	0.40	0.0514 - 0.0538	0.0526	0.0536 ± 0.0017	0.0530 ± 0.0005
7	0.1484	0.61	0.0518	0.39	0.0486 - 0.0534	0.0510	0.0513 ± 0.0020	0.0503 ± 0.0005

The mole fraction of the main InAsBi composition is greater than all the sideband InAsBi mole fractions for all samples except Samples c and g where the main composition mole fraction is greater than 85% and 77% respectively of the sideband composition mole fractions (see Fig. 21a). Furthermore, as the average in-plane strain decreases, the volume of InAsBi alloyed in the main composition increases weakly and both the main and sideband Bi mole fractions increase steadily (see Fig 21b). This suggests that the lateral compositional variation arises during growth due to the following opposing tendencies: (i) the mitigation of InAsBi in-plane tensile strain by the incorporation of Bi, resulting in the main InAsBi composition having a greater Bi mole fraction than the sideband composition in Samples a, b, d, e, and f, and (ii) the attainment of thermodynamic stability by limiting the incorporation of Bi, resulting in the range of sideband compositions.

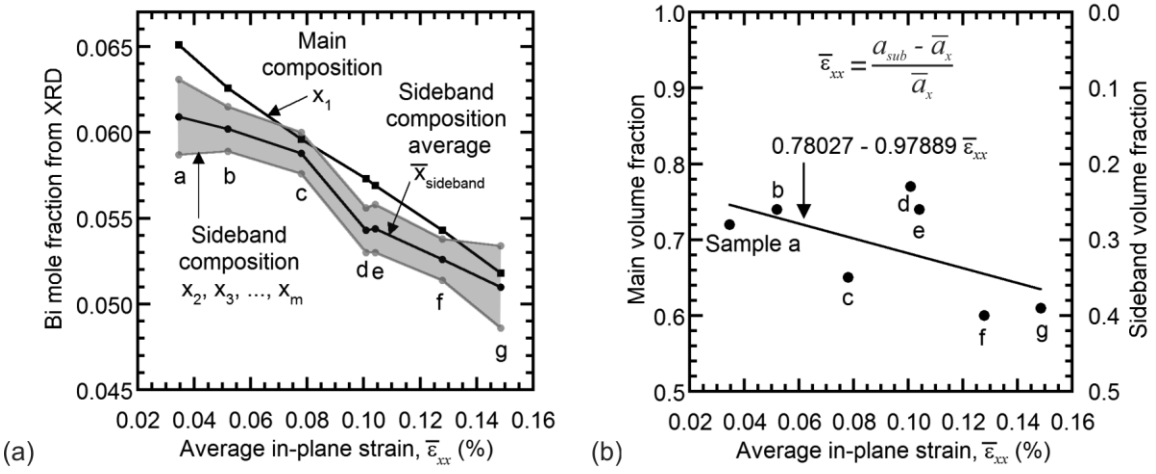

Figure 21. (a) Lateral distribution of Bi mole fraction and (b) volume of InAsBi in the dominant main composition (left-hand vertical axis) and the sideband composition (right-hand vertical axis) plotted as functions of in-plane strain. The equation for the in-plane strain is indicated in (b).

Thermodynamic calculations indicate that the solid solubility of InBi in InAs is < 0.025% and that this material system has a large miscibility gap [11], due in part to an increase in the substitution energy as a result of the strain introduced by the larger Bi atom [25]. During typical molecular beam epitaxy growth of III-V compounds at 400 to 700 °C, deposited Bi has a tendency to float on and evaporate from the surface without forming Bi droplets, making it an excellent surfactant. Nevertheless, InAsBi with Bi mole fractions well beyond the thermodynamic solubility limit are achieved using non-equilibrium molecular beam epitaxy growth [7] around 270 to 280 °C and organometallic vapor phase epitaxy growth [11] around 375 to 400 °C. Furthermore, strain driven composition variation has been observed in the growth direction of compressively strained III-V materials, including GaAsSb [26], InAsSb [26], GaAsBi [27], and InAsBi [Dominguez]. On the other hand, the tensilely strained InAsBi samples studied in this work exhibit lateral compositional variation that is perpendicular to the growth direction. These results indicate that Bi does not uniformly incorporate into the group-V sublattice under the near stoichiometric fluxes utilized to achieve the incorporation of Bi into the studied samples without the formation of surface Bi droplets [7].

Weak fringes that have an angular separation of ~20 arcsecond are observed in the XRD pattern for Samples a, d, e, and f and shown in Fig. 22; the fringes arise from the interference between X-rays reflected from the front and back interfaces of the 1 μm thick InAsBi layer.

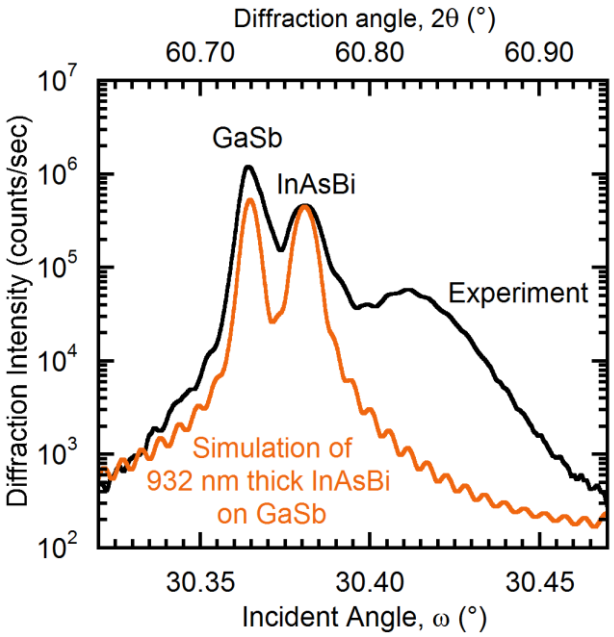

Figure 22. Interference fringes observed in (004) plane X-ray diffraction measurement of InAsBi on GaSb (Sample a) shown as a solid black curve, and simulation shown as a solid orange curve.

From ray optics, thickness of an epilayer t can be determined from the fringe peak angle θ_n, the spacing between the nth and (n+1)th diffraction fringes $(\Delta\theta)_n = \theta_{n+1} - \theta_n$, the angle between the incident X-ray beam and the sample surface θ, and the X-ray wavelength λ by using the first-order expression for the epilayer thickness is given in Equation 2.18.

$$t = \frac{\lambda}{2\cos\theta_n\,(\Delta\theta)_n} \tag{2.18}$$

The fringe peak angles are determined from the experiment data by fitting Gaussians. The InAsBi epilayer thickness is determined for Samples a, d, e, and f from the XRD diffraction fringe spacing using Equation 2.18 and summarized in Table VI.

The InAsBi epilayer thickness determined from the diffraction fringe spacing is in strong agreement with the thickness determined using RBS for Samples a and d, and in poor agreement for Samples e and f due to low X-ray diffraction signal at the fringe positions.

Table VI: Thickness of InAsBi layer determined using the spacing of fringes observed in X-ray diffraction data, and using Rutherford backscattering spectrometry.

Sample	InAsBi layer thickness (nm)	
	From XRD fringe spacing	From RBS
a	912	932
d	1043	927
e	811	938
f	501	944

As discussed earlier, vertical stripe features are observed in the bright-field cross-sectional transmission electron micrograph of Sample a (see Fig. 11b); these are attributed to the in-plane compositional variation of bismuth in the InAsBi epilayer on the order of 10 nm [21]. Diffraction fringes may arise in the XRD pattern from these vertical stripe features. Treating the vertical stripe features as thin films, an analysis of the interference of X-rays reflected from the front and back vertical interfaces results in Equation 2.19.

$$\Delta\theta \cong \frac{\lambda}{2d_{stripe}\tan^2\theta\sin\theta} \tag{2.19}$$

Using 10 nm for the vertical stripe thickness d_{stripe}, 0.154056 nm for the X-ray wavelength λ, and 30.4° for the incident angle θ, a diffraction fringe spacing of 0.25° is obtained. Fringes with such a large spacing are not observed in the XRD patterns.

2.4. Chapter 2 Summary

The structural properties of several nearly-lattice matched bulk InAsBi layers grown on GaSb substrates by molecular beam epitaxy are examined using X-ray diffraction and random and ion channeling Rutherford backscattering spectrometry. The random Rutherford backscattering spectrometry measurements indicate that the average Bi mole fraction of the samples range from 5.03% to 6.45% and the X-ray diffraction measurements indicate that the corresponding average lattice constants range from 6.0865 Å to 6.0935 Å. Analysis of these results indicates that the InBi lattice constant is 6.6107±0.0028 Å. Observed sidebands in the X-ray diffraction pattern confirm the presence of small variations in the lateral Bi composition that have been observed in cross-sectional transmission electron micrographs. Analysis of the main and sideband diffraction intensity indicates that approximately 70% of the InAsBi alloy is of a single composition, while the remaining 30% has a narrow range of compositions that are few tenths of percent lower on average.

3 MEASUREMENT OF BISMUTH SITE DISTRIBUTION IN BULK INASBI USING ION-CHANNELING

The presence of interstitials is detrimental to the performance of optoelectronic materials. During the growth of InAsBi, Bi atoms may incorporate at interstitial sites due to poor miscibility since the theoretical solid solubility limit of Bi in InAs is ~0.02 at.% at temperatures up to 400 °C [11]. In this chapter, the location of Bi atoms in InAsBi crystals using ion-channeling is discussed.

In Chapter 2, the principles of Rutherford backscattering are explained assuming that the ion beam probes a large fraction of sample atoms present in the uppermost layers of the sample (see Fig 23a and 23e). When the ion beam is aligned with a high-symmetry crystal direction, the ions are steered into the lattice through a series of small-angle, screened Coulomb collisions between the ions and the channel walls [28,29]. Consequently, a significant fraction of the crystal atoms are shadowed from the ion beam. This phenomenon is called ion-channeling. During channeling, less than 1% of the ions are scattered by the surface layer, less than $\sim 10^{-9}$ of the ions are scattered by each subsequent atomic layer, the ion beam flux is nearly constant up to a few microns into the crystal [30], and. a drop in the backscattering yield of at least an order of magnitude when compared to rotating random backscattering is observed (see 23b and 23f).

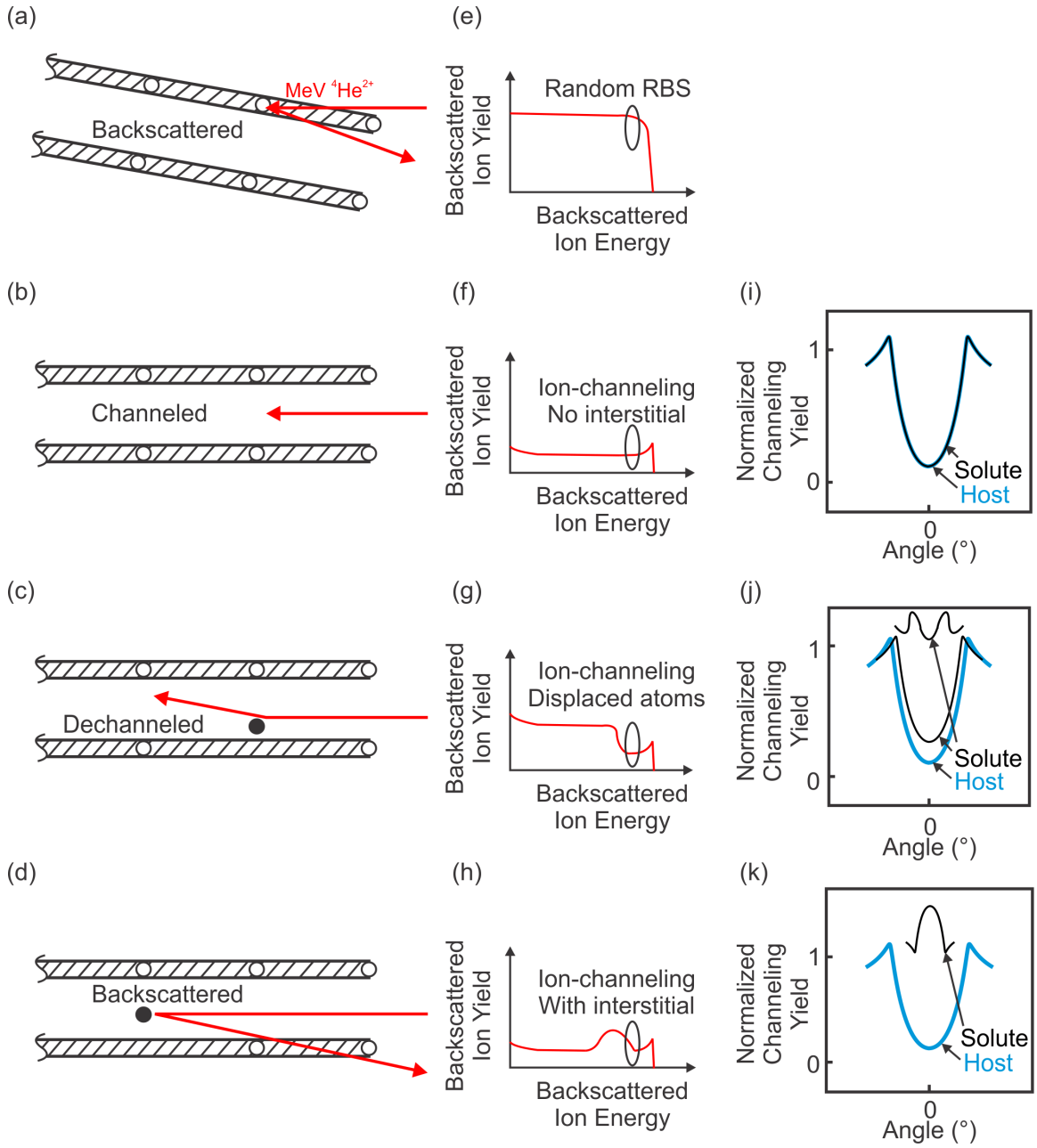

Figure 23: (a)-(d) Different geometries of incident ion beam with respect to crystal channels. The open black circles represent lattice atoms at substitutional sites, whereas the solid black circles represent lattice atoms at interstitial sites. (f)-(h) Random RBS or ion-channeling spectra. The ellipses indicate the backscattered ion beam energy at which normalized channeling yields are determined. (i)-(k) Normalized channeling yield plotted versus incident beam angle with respect to channel direction. (RBS and ion-channeling spectra adapted from [31])

Regardless of ion beam alignment with the sample or the material crystalline quality, a peak always arises in the ion-channeling spectrum as a result of backscattering from surface atoms (see Fig. 23f). Interstitial atoms or defects present in the crystal channel will dechannel (see 23c and 23g) or backscatter (see 23d and 23h) the incoming ion beam particles, leading to increased backscattered ion yield or appearance of extra peaks in the spectrum.

Normalizing channeling yields of interest to the corresponding random backscattering yield provides the curves shown in Fig. 23i, 23j, and 23k. For a sufficiently high density of displaced atoms the backscattered yield can be as large as the random yield [32], in which case the normalized channeling yield is close to unity. By comparing the normalized yield curve of the alloying element with that of the host, crystalline quality and defect distribution of crystalline samples can be characterized.

3.1. Samples Studied

Samples a, c, d, e, and f are examined using RBS ion-channeling along the <100> and <110> crystal directions. The sample information is listed in Tables II, V, and VII. Immediately after taking channeling measurements, a reference random RBS measurement is taken by tilting the sample 5° away from the ion channel axis in an arbitrary direction while rocking the sample about the normal.

Table VII: Growth details for the bulk InAsBi samples studied using ion-channeling.

Sample	Growth temperature (°C)	Bi/In flux ratio	As/In flux ratio
a	280	0.065	0.96
c	270	0.065	1.00
d	280	0.060	1.00
e	280	0.060	1.03
f	280	0.060	1.00

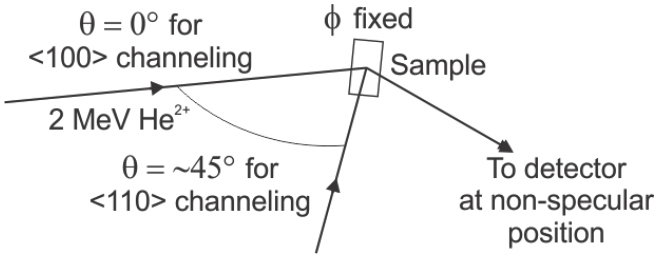

Figure 24: Sample setup during the ion-channeling measurements. θ is the incident angle with respect to the sample normal and ϕ is the azimuthal angle. The sample is not rotated during ion-channeling measurements, since this may cause dechanneling.

3.2. Ion-channeling

The ion-channeling measurements performed on Sample a are shown in Fig. 25. Those taken in the vicinity of the <100> channel are specified in (a) and those for the <110> channel are specified in (c); these measurements are presented as solid multicolored curves. The ion-channeling spectrum with the minimum backscattered ion yield is assigned an incidence angle of 0.0°. The backscattered ion yield increases as the sample is tilted away from the aligned orientation; the angular deviation from zero is

indicated for each curve. Three energy regions of the backscattered ion spectrum are examined further and are indicated by three vertical dashed lines at which the Bi, In+Bi, and As+In+Bi backscattered ion yields are minimum. These ion yields correspond to backscattering from the same depth below the upper InAsBi/InAs interface. The three channeling yields of interest are normalized to the random backscattering yield measured 5° out of alignment; see solid black curves in (a) and (c). The normalized channeling yields for these three regions are plotted as a function of angle in (b) for the <100> channel and (d) for the <110> channel. The Bi yield is shown as open red circles, the In+Bi yield as solid grey circles, and the As+In+Bi yield as open blue squares. The ion-channeling normalized yield curve exhibits a minimum when the ion beam is in line with the channel axis, increases as the crystal is tilted due to backscattering from atoms in the channel walls, and reaches a constant value a few degrees off-channel. The normalized yield curves for the remaining InAsBi samples (Samples c, d, e, and f) are shown in Fig. 26.

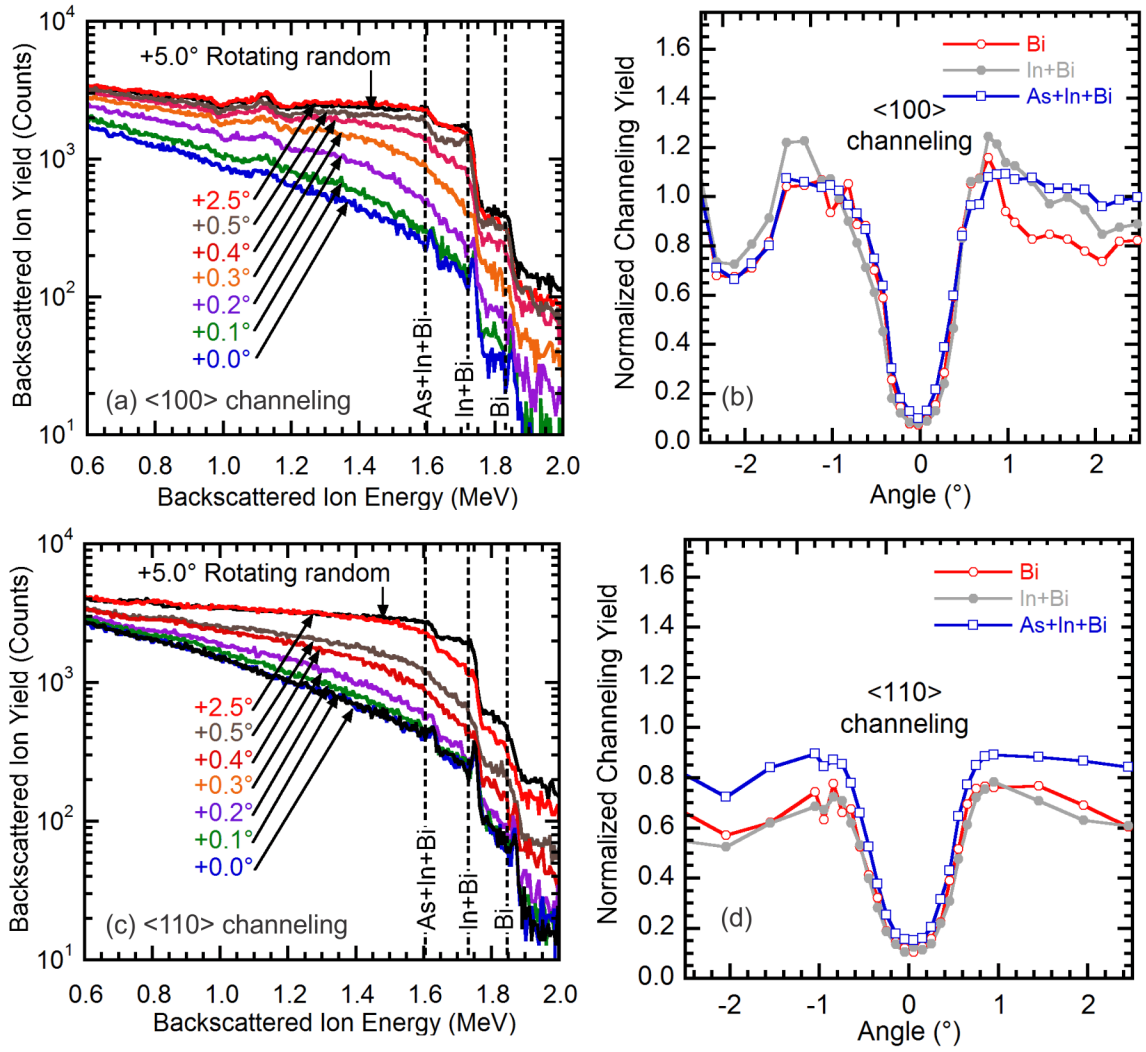

Figure 25. Rutherford backscattering measurements and normalized channeling yield curves for bulk $InAs_{0.935}Bi_{0.065}$ on GaSb (Sample a). Random measurements (see solid black curves) and ion-channeling measurements (see solid multicolor curves) are shown in (a) for the <100> channel and (c) for the <110> channel. The vertical dashed lines indicate the ion energies at which the Bi, In+Bi, and As+In+Bi backscattered ion yields are minimum. The ion-channeling measurements are normalized to random measurements.

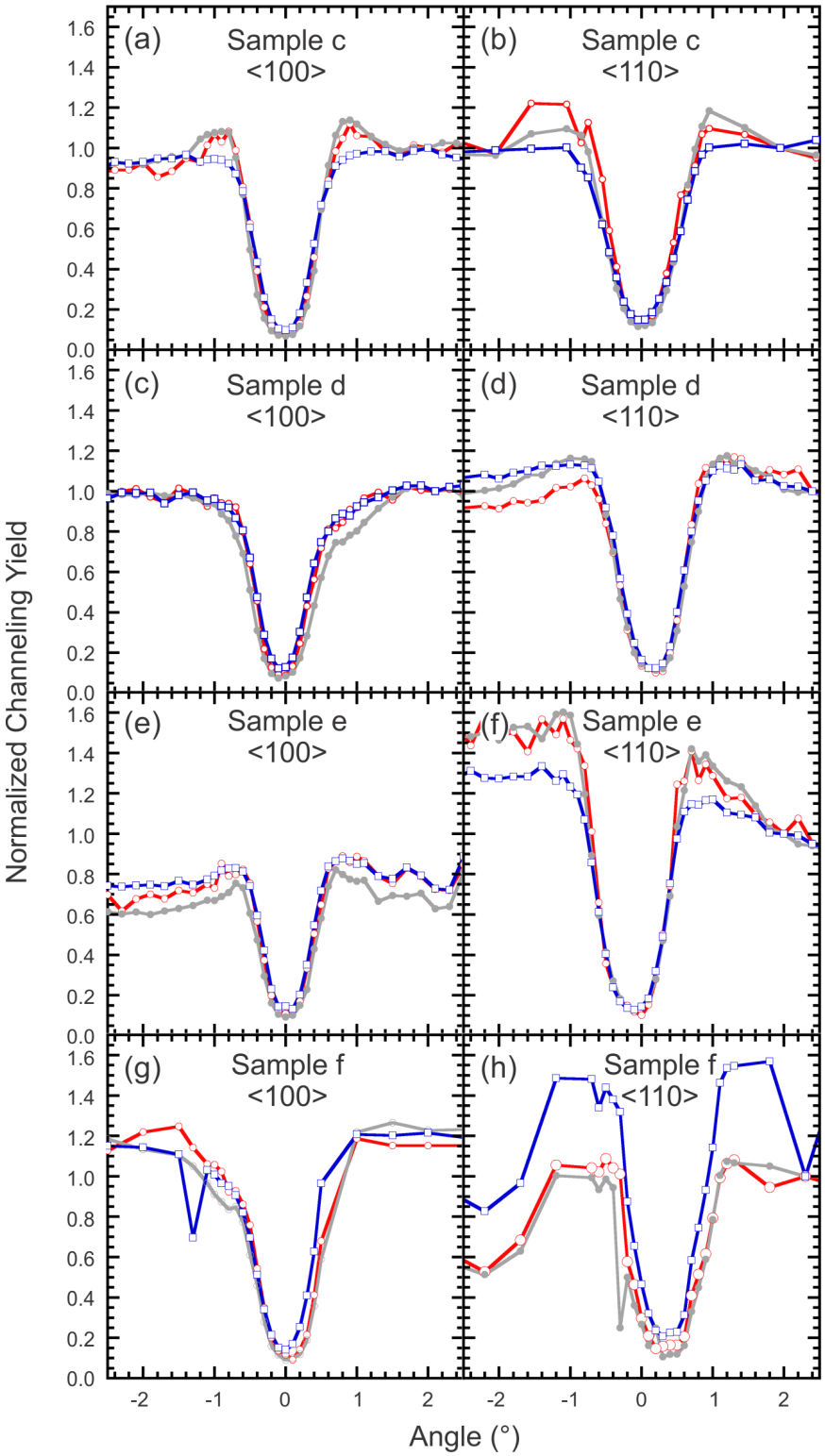

Figure 26. Normalized channeling yield curves of bulk InAsBi on GaSb (Samples c, d, e, and f) for <100> and <110> channeling.

Theoretical calculations indicate that displacement of Si crystal atoms by 0.1 Å into the <110> channel leads to a 0.2 decrease in normalized yield curve width [34]. The width of the normalized yield curves for Bi, In+Bi, and As+In+Bi are roughly the same at 0.9°±0.1° for all samples indicating that the Bi atoms are not displaced from the crystal lattice sites. The presence of a thin 10 nm cap layer (InAs or GaSb) on Samples a, c, d, and e has a negligible effect on the channeling measurements; simulation of the random spectra for these samples shows that the presence of a cap layer shifts the Bi signal to higher energy by only about 0.007 MeV.

The normalized yield curves for Bi, In+Bi, and As+Bi+In are obtained for all of samples a, c, d, e, and f (see Fig. 25 and 26). The minimum or zero angle values for each curve are determined by fitting an inverted Gaussian to the data in the range ±2.5° (see Fig. 27), and are shown as a function of sample Bi mole fraction in Fig. 28, with <100> channeling plotted in (a) and <110> channeling plotted in (b). The normalized minima for Bi, In+Bi, and As+In+Bi are similar for all samples. The minimum for As+In+Bi ranges from 0.10 to 0.14 for <100> channeling and 0.09 to 0.15 for <110> channeling and is slightly larger than that for Bi or In+Bi. For a sufficiently high density of displaced atoms the backscattered yield can be as large as the random yield and the normalized channeling yield close to unity. Since that is not the case for these results, little or none of the Bi atoms are interstitial.

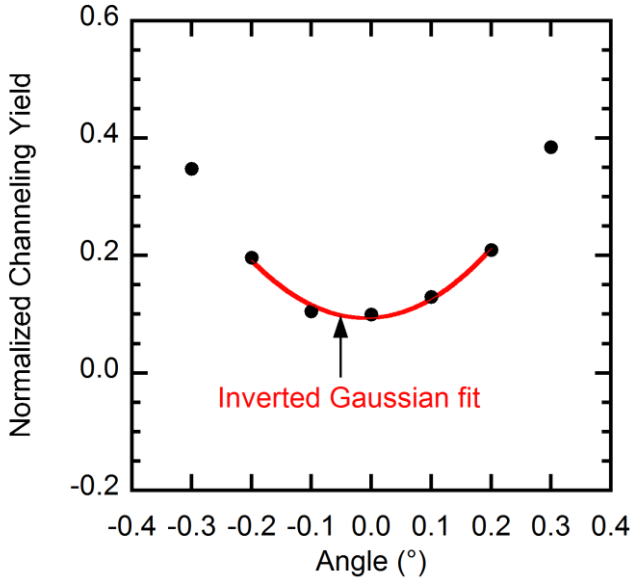

Figure 27. Parameterization of Bi normalized channeling yield minimum for <100> channeling of InAsBi (Sample 1) using an inverted Gaussian function.

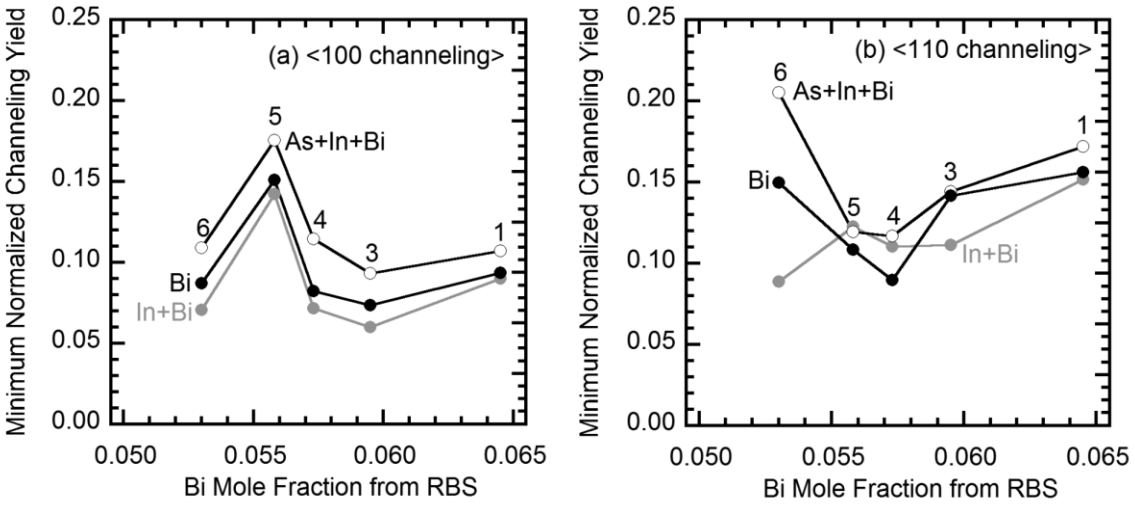

Figure 28. Normalized channeling yield minimum (left-hand vertical-axes) and angular width (right-hand vertical-axes) for bulk InAsBi on GaSb as a function of sample Bi mole fraction; <100> channeling shown in (a) and <110> channeling shown in (b). The yield for Bi is indicated by the solid black squares, In+Bi by the solid grey squares, and As+In+Bi by the open black circles.

For comparison, the normalized yield minimum for InAs is 0.04 for <100> channeling and 0.03 for <110> channeling, for GaAs is 0.05 for <100> channeling and 0.04 for <110> channeling [35], for GaInAs is 0.05 for <100> channeling and 0.15 for <110> channeling [36], and for GaInP is 0.26 for <100> channeling [37]. In general binaries have smaller channeling yield minimums compared to ternaries. Furthermore, since the normalized yield minimum of the bulk InAsBi samples studied is similar to those for other ternaries, the degree of crystalline quality is expected to be comparable with these materials.

Since Bi atoms are substituted for As atoms in the group-V sublattice of the InAsBi crystal, the normalized channeling yield from Bi would ideally be compared with that from As, or both As and In. However, the normalized yield curves for As or As+In cannot be determined since both the As and In signals coincide with the Bi signal (see simulation breakdown in Fig. 17). The normalized channeling yield from Bi has been compared to In alone for 300–500 nm thick InAsBi layers in other published work [33]. For the samples studied here, the InAsBi layer is 1000 nm thick and the In normalized yield cannot be independently determined due to signal overlap.

Since the backscattered yield is proportional to atomic mass squared, about 91% of the As+In+Bi signal is from As and In atoms which constitute about 96% of the total atoms. This makes As+In+Bi the best available choice for a reference to analyze the Bi yield. Alternatively, the difference between the As+In+Bi and In+Bi normalized yield would be an estimate of the As normalized yield.

A first-order estimate of the fraction of substitutional solvent atoms is provided by the following expression [32].

$$\text{Substitutional fraction} = \frac{1 - \chi_{solvent}}{1 - \chi_{host}} \quad ; \tag{3.1}$$

where, χ is minimum normalized channeling yield for each channeling direction. The substitutional fraction of Bi atoms for the samples is calculated using this equation and shown in Fig. 29 as a function of Bi content, where the solvent is χ_{Bi} and the host is $\chi_{As+In+Bi}$ in (a), $\chi_{As+In+Bi} - \chi_{In+Bi}$ in (b), and χ_{In+Bi} in (c), as indicated in each plot. The substitutional fraction along <100> is shown as solid black circles and the substitutional fraction along <110> is shown as solid grey squares. Calculations done using $\chi_{As+In+Bi}$ indicate that all Bi atoms are substitutional (> 100%), whereas $\chi_{As+In+Bi} - \chi_{In+Bi}$ indicates 86–96% and χ_{In+Bi} indicates 93–103% and both have a wider less consistent range of values. The range of these results indicates that the measurement and analysis has a limited sensitivity. Nevertheless, the normalized yield with As+In+Bi as the host is the most consistent result and indicates that the Bi atoms are substitutional.

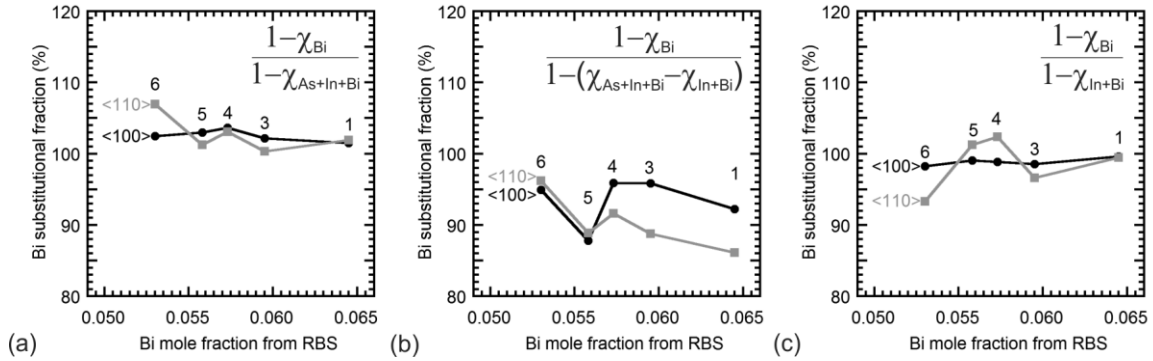

Figure 29. Fraction of Bi atoms that are substitutional in bulk InAsBi as a function of Bi mole fraction (Samples a, c, d, e, and f), using various combinations of the host normalized yield minima, where the solvent is χ_{Bi} and the host is $\chi_{As+In+Bi}$ in (a), $\chi_{As+In+Bi} - \chi_{In+Bi}$ in (b), and χ_{In+Bi} in (c). The solid black circles indicate <100> channeling and solid grey squares indicate <110> channeling.

3.3. Chapter 3 Summary

The ion channeling measurements indicate high-quality crystalline InAsBi with substitutional Bi atoms in all samples.

4 OPTICAL PROPERTIES OF InAsBi QUANTUM WELLS

Several high-quality dilute bismide InAs/InAsBi/InAs quantum wells are grown on GaSb substrates using molecular beam epitaxy. The optical properties of the quantum wells are investigated using temperature and excitation dependent photoluminescence spectroscopy. Analysis of the integrated photoluminescence as a function of carrier excitation density indicates radiative dominated recombination and high internal quantum efficiency over the 12 to 250 K temperature range. The InAsBi bandgap is determined from the photoluminescence spectra and parameterized as a function of temperature using Einstein single oscillator model. The dilute Bi mole fraction of the InAsBi quantum wells is determined by comparing the measured bandgap energy to that predicted by the valence band anticrossing model. The Bi mole fraction of the InAsBi quantum wells measured independently using secondary ion mass spectrometry agrees reasonably well with that determined by photoluminescence.

4.1. Samples Studied

Coherently strained InAsBi quantum well structures consisting of a 500 nm thick GaSb buffer, a 10 nm thick AlSb barrier, a 50 nm thick InAs confinement layer, a 10 nm thick InAsBi quantum well, a 50 nm thick InAs confinement layer, a 10 nm thick AlSb barrier, and a 10 nm thick GaSb cap are grown using molecular beam epitaxy on (100)-oriented p-type GaSb substrates [7]. A total of 5 quantum well samples are produced and summarized in Table VIII. The InAsBi layers in each sample are grown at 300 °C using a Bi/In flux ratio of 0.021 and As/In flux ratios ranging from 0.97-1.04. The InAs

confinement layers are grown using an As/In flux ratio of 1.30 to ensure that any remaining surface Bi is not incorporated outside of the quantum well. Sample 6 consists of a 500 nm thick GaSb buffer, a 10 nm thick AlSb barrier, a 110 nm thick InAs layer, a 10 nm thick AlSb barrier, and a 10 nm thick GaSb cap. This structure is essentially the quantum well sample structure grown with a constant As/In flux ratio of 1.30 and no Bi, and serves as a reference for the photoluminescence analysis.

Sample g is the bulk InAsBi sample consisting of a 500 nm thick GaSb buffer, a 15 nm thick InAs layer, and a 1 μm thick $InAs_{0.95}Bi_{0.05}$ layer whose sample information is provided in Tables II, V, and VII. Sample g is utilized to calibrate Bi mole fraction measurements using secondary ion mass spectrometry (SIMS).

Table VIII: Growth conditions for InAsBi quantum well and bulk layers. Samples 1 through 5 are 50 nm InAs/10 nm InAsBi/50 nm InAs quantum well (QW) structures, Sample 6 is a 110 nm thick layer of tensilely strained InAs layer containing no Bi, and Sample g is a 1 μm thick layer of $InAs_{0.95}Bi_{0.05}$.

Sample	Type	Growth temperature (°C)	Bi/In flux ratio	As/In flux ratio
1	QW	300	0.021	1.04
2	QW	300	0.021	1.00
3	QW	300	0.021	1.01
4	QW	300	0.021	0.98
5	QW	300	0.021	1.00
6	Bulk	300	0.000	1.30
g	Bulk	280	0.060	1.05

4.2. Photoluminescence Spectroscopy

Photoluminescence emission from Samples 1 through 6 is measured as a function of temperature (12-295 K) and pump power (0.7 to 200 mW) using an 808 nm wavelength pump laser with spot diameter of 183 μm, a liquid nitrogen cooled InSb detector, and a 16 cm^{-1} (or 2 meV) spectral resolution Nicolet Instrument Corporation Magna-IR 760 Fourier transform infrared spectrometer. The pump power density reaching the active region of each sample is 0.93 to 265 W cm^{-2}, which corresponds to an excitation density range of 2×10^{24} to 5×10^{26} cm^{-3} s^{-1}. The samples are mounted within a closed loop helium cryostat and pump power dependent photoluminescence measurements are performed on the samples by fixing the sample temperature and varying the pump powers, set using a variable neutral density filter.

The photoluminescence measurements taken on Samples 1, 5, and 6 at 12 K are shown as a function of photon energy and pump power density in Fig. 30. In the plots, each curve indicated in black represents an order of magnitude increase in the pump power. For measurements performed on each sample, increasing excitation results in a larger photoluminescence intensity and a shift in the photoluminescence peak position to higher energies. Comparing the photoluminescence spectra in Fig. 30 (a), (b), and (c) a shift in the photoluminescence peak position and the extent of the Urbach tail to lower energies is observed. This shift confirms the incorporation of Bi and is generally attributed to localized states in the vicinity of the valence band due to dilute quantities of Bi, which has previously been observed in GaAsBi [38,39].

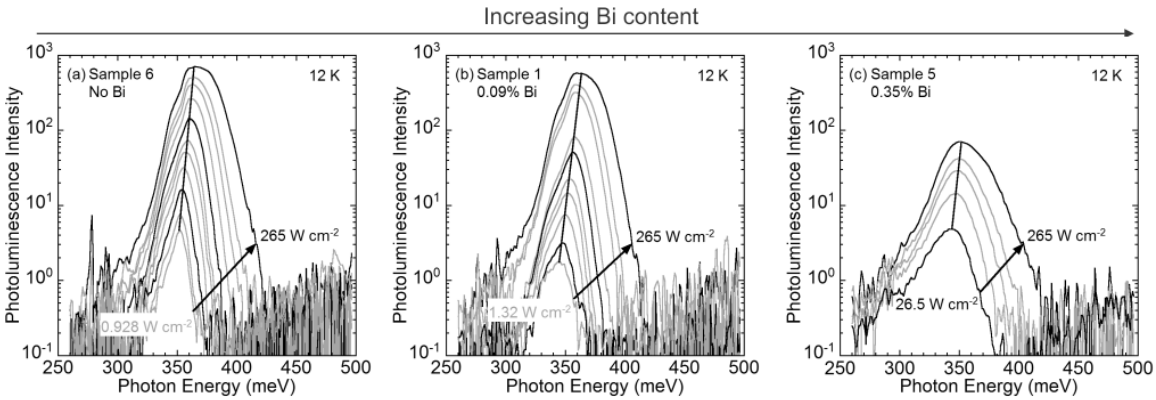

Figure 30. Photoluminescence spectra from InAs on GaSb (Sample 6) and InAsBi/InAs quantum wells on GaSb (Samples 1 and 5) at 12 K, measured using pump power densities ranging from 0.928 W cm^{-2} to 265 W cm^{-2}. The arrows overlaying the spectra indicate increasing pump power densities and the slanted lines is a guide to the position of the peak maxima.

An accurate method of identifying the bandgap from the photoluminescence is required to determine the temperature dependence of the InAsBi bandgap. The shape of the photoluminescence spectrum is a function of the optical joint density of states, which is the number of states available in the vicinity of the optical transition, and the photon occupation number, which is a parameter that quantifies the extent to which a state is filled. Maximum change in the optical joint density of states occurs at the bandgap energy. Further, at the bandgap the rate of increase of the optical joint density of states is much more rapid than the rate of decrease of the occupation number. Thus the maximum change in the optical joint density of states and therefore the fundamental bandgap energy is identified as the as the maximum of the photoluminescence first derivative; the first derivative maximum correctly identifies the bandgap energy in the idealized case of a perfectly sharp band edge cutoff specified by the parabolic band model [40].

The bandgap energy is determined for the studied samples using the first derivative method and the results for Samples 1, 5, and 6 are shown in Fig. 31 as a function of pump power density and temperature. The reduction in the bandgap between the reference sample containing no Bi (Sample 6) and the samples containing bismuth (Samples 1 through 5) provides a measure of the overall bandgap reduction due to bismuth. At low temperature and low injection, the photoluminescence first derivative maxima indicate an apparent narrowing of the bandgap energy with decreasing pump power; this redshift is evidence for the filling of unoccupied states just below the bandgap energy. At low excitation conditions the bands are simply not filled up to the bandgap due to insufficient pump power. As the excitation density is increased, the localized states are saturated and the photoluminescence emissions are increasingly dominated by band-to-band recombination, resulting in saturation of the bandgap energy at temperatures above 100 K and injection levels greater than 60 W-cm^{-2} for all the studied samples.

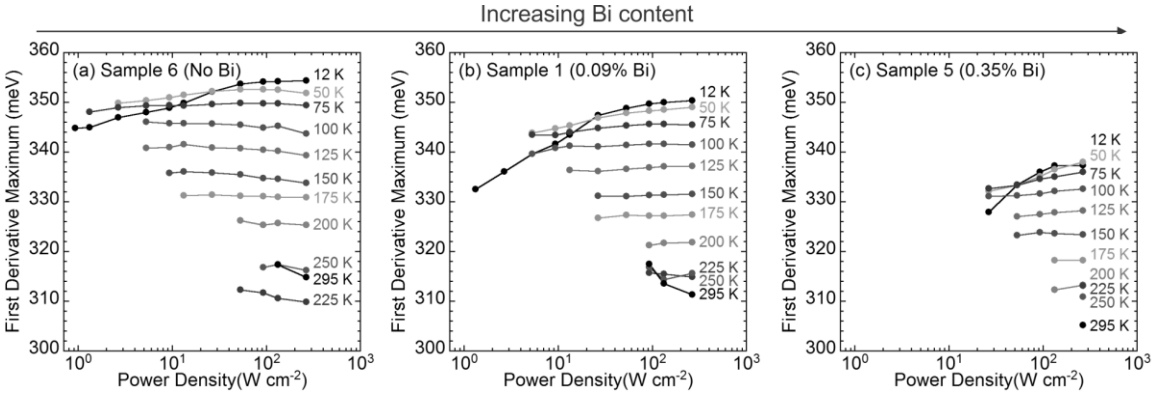

Figure 31. First derivative maximum of InAs (Sample 6) and InAsBi quantum wells (Samples 1 and 5) determined from the photoluminescence results, shown as a function of pump power density and temperature.

The bandgap energy of each sample is aggregated over pump power densities greater than 90 W photoluminescence measurements and plotted as a function of temperature in Fig. 32. In the figure, solid circles identify low temperature (≤ 200 K) bandgap energy that are accurately determined, and unfilled circles identify high temperature (> 200 K) bandgap energy that have significant uncertainty. The uncertainty in the aggregated bandgap energy is large for high temperature measurements, which have small output photoluminescence intensity, and decreases when output photoluminescence intensity increases, which occurs as temperature decreases. The Einstein single oscillator function [41,42] given in Equation 4.1 is fit to the low temperature (≤ 200 K) bandgap energy E_g of each sample.

$$E_g = E_0 - \frac{SkT_E}{\exp(T_E/T) - 1} \tag{4.1}$$

where, E_0 is the InAsBi bandgap at 0 K, S is the coupling parameter, k is the Boltzmann constant (0.08617 meV/K), T_E is the Einstein temperature, and T is the measurement temperature, and Sk is the slope of the high temperature linear asymptote. The fit of the Einstein single oscillator function is performed excluding the high temperature bandgap energy data (> 200 K) due to the high level of variance in the photoluminescence spectra at high temperature. The best-fit parameter values are summarized in Table IX. The Einstein temperature T_E and the coupling parameter S, collectively called the Einstein parameters, increase steadily with increasing Bi mole fraction, as shown in the Fig. 32 inset. A larger Einstein temperature indicates that the knee in the temperature dependent

curves in Figure 32 will extend to the right, and a larger coupling parameter indicates that the bandgap will decrease at a greater rate in the linear asymptote region at temperatures greater than the Einstein temperature.

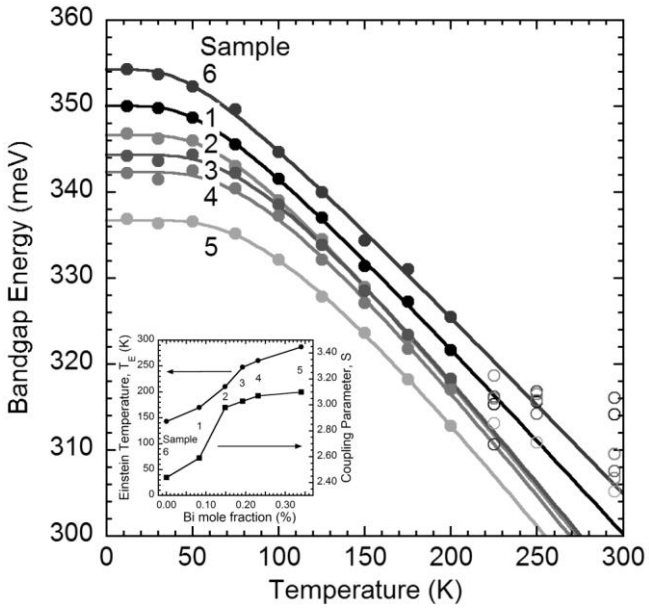

Figure 32. Bandgap energy of InAs (Sample 6) and InAsBi quantum wells (Samples 1 through 5), aggregated over the three largest pump power density measurements, and plotted as a function of the measurement temperature. The solid black curves are the best fits of the Einstein single oscillator model function (Equation 4.1) to the low temperature (≤ 200 K) data set for each sample, shown as solid black circles. The high temperature (> 200 K) data are shown as hollow black circles and are excluded from the fits, as the uncertainty in the values is large. The inset shows the trends in the Einstein temperature T_E (left-hand vertical axis) and the Coupling parameter S (right-hand vertical-axis) with bismuth content (lower horizontal-axis).

Table IX: Einstein single oscillator model parameters that best fit the temperature dependence of the InAs and InAsBi bandgap energy, and Bi mole fraction of the samples determined using photoluminescence spectroscopy (PL) and secondary ion mass spectrometry (SIMS). E_0 is the bandgap energy at 0 K, E_{295} is the bandgap energy at 295 K, S is the coupling parameter, and T_E is the Einstein temperature.

Sample	Bandgap energy at 0 K E_0 (meV)	Bandgap energy at 295 K E_{295} (meV)	Coupling parameter S	Einstein temperature T_E (K)	Bi mole fraction, x_{PL} (%)	Bi mole fraction, x_{SIMS} (%)
1	349.9	301.3	2.59	170.0	0.086	0.128
2	346.6	294.7	2.98	210.4	0.152	0.126
3	344.3	295.2	3.03	247.7	0.198	-
4	342.3	293.6	3.07	260.5	0.238	-
5	336.7	290.1	3.10	286.8	0.350	-
6	354.2	305.9	2.44	143.1	0.000	0.000

The bandgap energy of InAsBi at 0 K is calculated using the valence band anticrossing model [43]. In the model, the Bi coupling parameter characterizes the InAsBi valence band edge position as a function of Bi mole fraction while the conduction band edge varies linearly with mole fraction between the conduction band edge positions of InAs and InBi. The bandgap energy of bulk $InAs_{0.935}Bi_{0.065}$ is measured using spectroscopic ellipsometry from which the 1.529 eV Bi coupling parameter is determined [3], which produces the solid curves shown in Fig. 33. The mole fractions at which InAsBi is lattice-matched to InAs and GaSb are marked in the figure by vertical black and grey dashed lines respectively. Departing from these lattice-matched compositions, strain acts to shift the conduction and valence bands and splits the degenerate heavy and light hole band edges. This results in the strained InAsBi bandgap energy curves for growth on GaSb (solid black curve) plotted as functions of Bi mole fraction (lower

horizontal-axis) and strain (upper horizontal-axes) in Fig. 33. For the bandgap of strained material, optical transitions involve the light hole band for positive values of strain and the heavy hole band for negative values of strain.

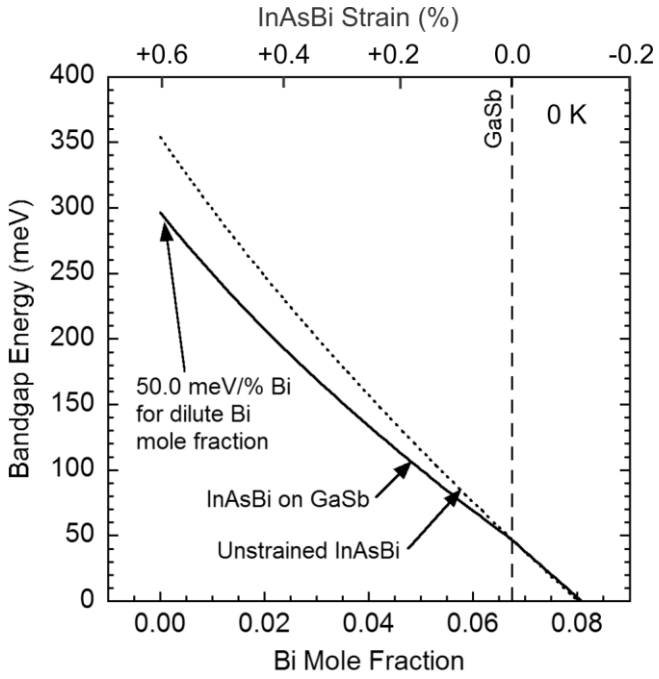

Figure 33. Low-temperature bandgap energy of InAsBi as a function of Bi mole fraction. The solid black curve shows the bandgap of InAsBi pseudomorphically strained on GaSb, plotted versus Bi mole fraction (lower horizontal-axis) and layer strain (upper horizontal-axes). The dotted black curve shows the bandgap of unstrained bulk InAsBi as a function of Bi mole fraction. The vertical dashed line shows the lattice-matched mole fraction (zero strain) for growth GaSb.

An average linear bandgap reduction rate of 50.0 meV per percent Bi is predicted with the valance band anticrossing model for InAsBi on GaSb containing dilute amounts of Bi as shown in Fig. 33. This bandgap reduction rate is in agreement with experimentally determined bandgap reduction rates of 42.0 meV per percent Bi and 55.0

meV per percent Bi reported in Refs. 33 and 9, wherein dilute InAsBi samples are examined. Using the experimentally determined bandgap energy of the studied samples at 0 K (E_0) and the linear bandgap energy reduction rate of 50.0 meV per percent Bi, the bismuth mole fraction of the InAsBi quantum well samples is determined using Equation 4.2 and summarized in Table IX.

$$x_{PL} = \frac{E_0(\text{meV}) - 354.2(\text{meV})}{50.0\ (\text{meV}/\%\ \text{Bi})} \tag{4.2}$$

The bandgap energy at 0 K (E_0, solid black circles) and 295 K (E_{295}, open black circles) of the studied samples are shown as functions of the bismuth mole fraction in Fig 34. The solid black lines represent bandgap energy reduction rates at 0 K (50.0 meV per percent Bi) and 295 K (50.9 meV per percent Bi) calculated using the band anticrossing model. The bandgap energy reduction rate at 295 K is in excellent agreement with the bandgap energy values determined by fitting the Einstein Single Oscillator model to the bandgap energy data.

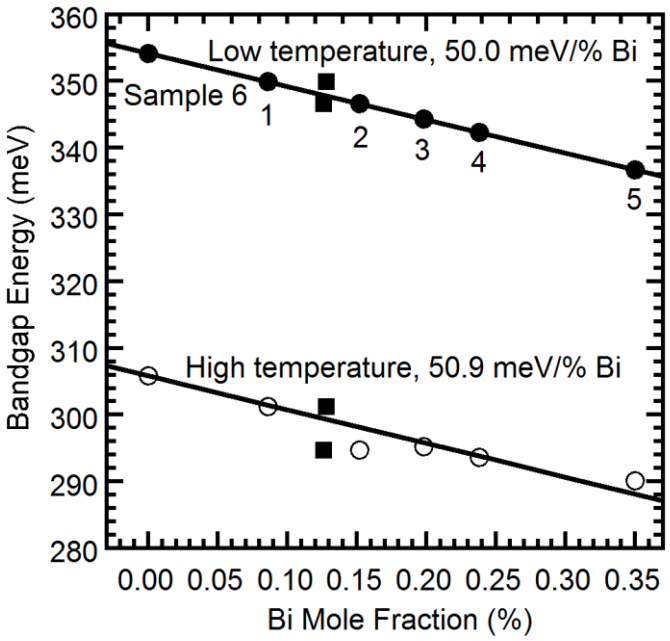

Figure 34. Bandgap energy of InAs (Sample 6) and InAsBi quantum wells (Samples 1 through 5) at 0 K (solid black circles) and at 295 K (open black circles) as functions of bismuth mole fraction. Both sets of bandgap energy are determined using Einstein single oscillator model fits to the overall temperature dependence of the bandgap energy for each sample. A linear bandgap reduction rate of 50.0 meV/% Bi at 0 K (upper solid black line) is used to determine the bismuth mole fraction of the InAsBi samples from the low temperature bandgap energy. Bandgap reduction rate of 50.9 meV/% Bi at 295 K is shown as the lower solid black line.

4.3. Secondary Ion Mass Spectrometry

Secondary ion mass spectrometry measurements of the InAsBi quantum well samples and the $InAs_{0.95}Bi_{0.05}$ reference standard are performed using a Cameca IMS 6f system, utilizing a 7.7 keV O^{2+} primary beam and detecting positive secondaries at 4.988 kV. The samples are milled to depths of ~150 nm. Measurement of the bulk $InAs_{0.95}Bi_{0.05}$ reference (Sample g) yields a signal of 1300 counts/s for the bismuth mole

fraction of 0.0503. For the InAsBi quantum wells, signals collected at atomic masses of 209 and 71 roughly track each other, as shown in Fig. 35. The secondary ion signal collected at atomic mass 209 is identified to be a combination of signals from Bi and from 3Ga, which is an ionic cluster having mass number 69+69+71 = 209. This signal is given by the open grey circles marked Bi+3Ga in Fig 35. The signal that uniquely arises from Bi only is isolated from the aggregate signal by subtracting away a scaled fraction of the Ga signal (atomic mass 71; solid black curve marked Ga). The bismuth signal is shown in Fig. 35 as a solid black curve. A peak is observed in the Bi signal at a depth of 70 nm at which the InAsBi quantum well is present. Integrating the area under the peak gives a yield of 2151 counts or 32.5 counts/s. Assuming that Bi mole fraction varies proportionally with secondary ion intensity, the mole fraction of the InAsBi quantum wells, x_{SIMS}, is determined using Equation 4.3 for Samples 1 and 2 and are summarized in Table IX.

$$\begin{aligned} x_{SIMS} = & \frac{\text{Reference Bi mole fraction}}{\text{Reference Bi secondary ion intensity}} \\ & \times \text{Quantum well secondary ion intensity} \\ & \cong 3.87 \times 10^{-5} \times \text{Quantum well secondary ion intensity} \end{aligned} \tag{4.3}$$

Additionally, the presence of a peak in the Bi signal at a milled depth of ~20 nm (see Fig. 35) suggests the presence of Bi at the upper AlSb/InAs interface, indicating that the Bi is readily incorporated once the As flux is terminated.

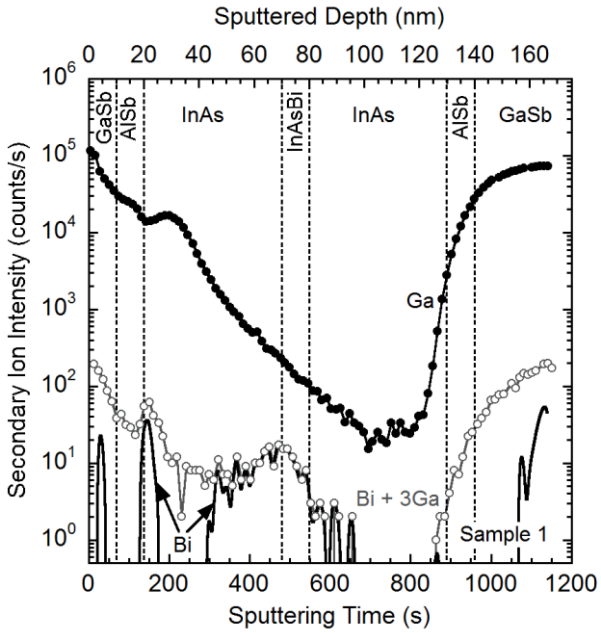

Figure 35. Secondary ion mass spectrometry measurements of InAsBi quantum well on GaSb (Sample 1) collected at atomic masses 71 (solid black circles marked Ga) and 209 (open black circles marked Bi+3Ga) as functions of measurement time (bottom horizontal-axis) and distance milled through the sample (upper horizontal-axis). As some of the signal at atomic mass 209 arises from 3Ga ionic clusters, a scaled fraction of the signal at atomic mass 71 (Ga) is subtracted away to obtain the signal from bismuth only (solid black curve). The vertical dotted lines indicate the depths at which interfaces are present between sample layers.

The integrated photoluminescence from the InAsBi quantum wells are plotted versus pump powers in Fig. 36, and are shown as solid circles. The photoluminescence spectra measured at low pump powers are unreliable due to noise. When bismuth is incorporated in the sample, the peak photoluminescence efficiency is observed near 50 K. This can be explained to be a result of thermal energy induced tunneling of carriers between tail states, causing them to be trapped in a localized radiative state; further

increase in temperature provides enough energy to move the trapped carriers to move into above bandgap states where they can move freely to find non-radiative centers [44].

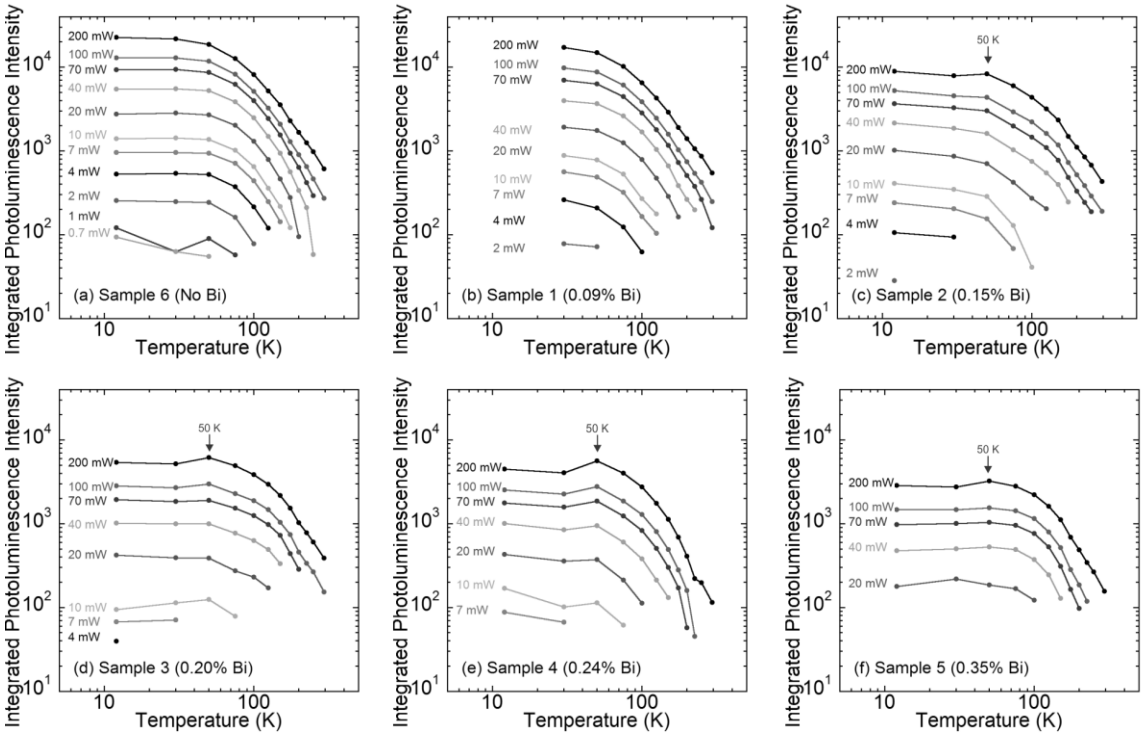

Figure 36. Integrated photoluminescence intensity versus temperature measured at various pump powers for bulk InAs (Sample 6) and InAsBi quantum wells (Samples 1 through 5). The peak photoluminescence efficiency is observed near 50 K for Samples 2 through 5.

Analysis of the integrated photoluminescence intensity as a function of temperature and excitation in Fig. 37 provides a measure of the optical quality of the InAsBi quantum wells. When recombination takes place mainly by radiative recombination, the integrated photoluminescence is proportional to the pump power and hence follows a power law 1 slope as a function of pump power. In contrast, when the

non-radiative or Shockley-Read-Hall recombination dominates, the integrated photoluminescence follows a power law 2 slope as a function of pump power [43]. The power law 1 and 2 slopes are indicated in Fig. 37 by dashed lines for comparison to the data. The quantum wells operate with near quantum efficiency (power law 1) over most temperatures and excitation densities, and follow non-radiative recombination at higher temperatures and lower excitation levels. This suggests that the InAsBi quantum wells operate with near-unity quantum efficiency over a significant range of pump powers and temperatures

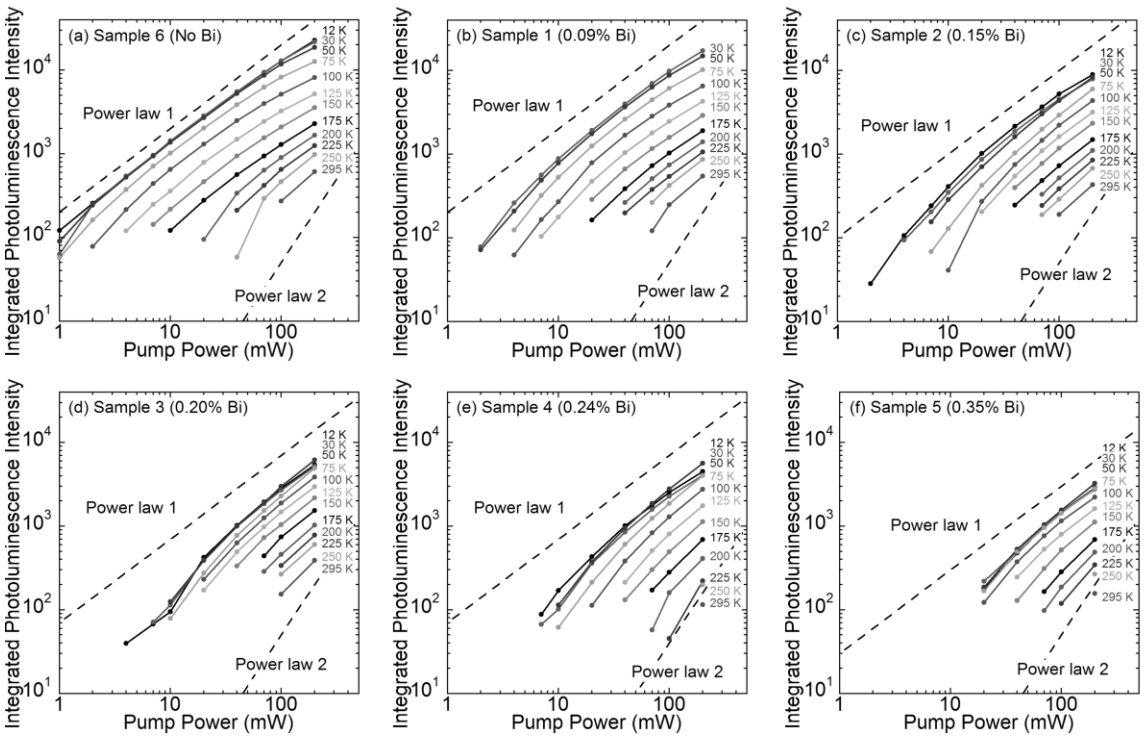

Figure 37. Integrated photoluminescence intensity plotted as a function of the pump power density used to excite bulk InAs (Sample 6) and InAsBi/InAs quantum wells (Samples 1 to 5) at temperatures ranging from 12 K to 295 K. Characteristic slopes for radiative (power law 1) and Shockley-Read-Hall (power law 2) limited recombination are indicated by dashed lines.

4.4. Chapter 4 Summary

InAsBi quantum well samples are studied using temperature and pump-power dependent photoluminescence. An analysis of the pump-power dependent photoluminescence measurements indicates that the recombination is radiative-limited over most temperatures and pump powers, suggesting good optical quality in the dilute bismide InAs/InAsBi/InAs quantum wells. Bi mole fraction in the quantum wells is determined using bandgap energy from photoluminescence measurements, and confirmed using secondary ion mass spectrometry.

5. CONCLUSIONS

Bulk InAsBi alloys are attractive candidates for direct gap highly-tunable mid- and long-wave infrared optoelectronic devices that can be grown on commercially-available binary substrates such as InAs and GaSb. In particular, InAsBi can be utilized as nearly lattice-matched bulk InAsBi, or as strained InAsBi quantum wells on GaSb.

Several thick InAsBi layers with Bi mole fractions ranging from 5.03% to 6.45%, nearly lattice matched to the underlying GaSb substrate are examined using Rutherford backscattering spectrometry and X-ray diffraction. Ion-channeling measurements confirm that the Bi atoms are substitutional in the InAsBi crystal. A lateral variation in the Bi mole fraction is observed where about 70% of the InAsBi has a single composition and the remaining 30% has a narrow range of slightly lower compositions. By modeling the main and sideband (004) diffraction peaks, the average out-of-plane tetragonal distortion is determined. The average unstrained lattice constant for the sample set ranges from 6.0865 Å to 6.0935 Å; comparing these to the Bi mole fraction determined by random Rutherford backscattering spectrometry, the InBi lattice constant is estimated to be 6.6107± 0.0028 Å.

The optical properties of InAsBi quantum wells containing dilute quantities of Bi and strained to GaSb lattice constant are assessed using photoluminescence. The InAsBi quantum wells exhibit radiative limited recombination over most temperatures and excitation levels.

REFERENCES

[1] R. A. Rohde, "Radiation Transmitted by the Atmosphere.Png" Global Warming Art http://www.globalwarmingart.com/wiki/File:Atmospheric_Transmission.png (accessed 03/14/2016).

[2] M. A. Kinch. *Fundamentals of Infrared Detector Materials, (Tutorial Texts in Optical Engineering),* vol. *TT76, 2007*.

[3] P. T. Webster, A. J. Shalindar, N. A. Riordan, C. Gogineni, H. Liang, A. R. Sharma, and S. R. Johnson, J. Appl. Phys. **119**, 225701 (2016).

[4] G. C. Osbourn, "InAsSb strained-layer superlattices for long wavelength detector applications," *J*. *Vac*. *Sci*. *Technol*. *B*, vol. 2, pp. 176, 1984.

[5] J. W. Matthews and A. E. Blakeslee, J. Cryst. Growth **27**, 118 (1974).

[6] A. Janotti, Su-Huai Wei, and S. B. Zhang, Phys. Rev. B **65**, 115203 (2002).

[7] P. T. Webster, N. A. Riordan, C. Gogineni, S. Liu, J. Lu, X.-H. Zhao, D. J. Smith, Y.-H. Zhang, and S. R. Johnson, J. Vac. Sci. Technol. B **32**, 02C120 (2014).

[8] P. T. Webster, N. A. Riordan, S. Liu, E. H. Steenbergen, R. A. Synowicki, Y.-H. Zhang, and S. R. Johnson, J. Appl. Phys. **118**, 245706 (2015).

[9] Z. M. Fang, K. Y. Ma, R. M. Cohen, and G. B. Stringfellow, J. Appl. Phys. **68**, 1187 (1990).

[10] B. Joukoff, and A. M. Jean-Louis, J. Cryst. Growth **12**, 169 (1972).

[11] K. Y. Ma, Z. M. Fang, R. M. Cohen, and G. B. Stringfellow, J. Cryst. Growth **107**, 416 (1991)

[12] H. Okamoto, and K. Oe, Jpn. J. Appl. Phys. **37**, 1608 (1998).

[13] Y. Gu, K. Wang, H. Zhou, Y. Li, C. Cao, L. Zhang, Y. Zhang, Q. Gong, and S. Wang, Nanoscale Res. Lett. **9**, 1 (2014).

[14] K. Wang, Y. Gu, H. F. Zhou, L. Y. Zhang, C. Z. Kang, M. J. Wu, W. W. Pan, P.F. Lu, Q. Gong, and S. Wang, Sci. Rep. **4**, 5449 (2014).

[15] M. K. Rajpalke, W. M. Linhart, K. M. Yu, M. Birkett, M. Birkett, J. Alaria, J. J. Bomphrey, S. Sallis, L. F. J. Piper, T. S. Jones, M. J. Ashwin, and T. D. Veal, Appl. Phys. Lett. **105**, 212101 (2014).

[16] I. Vurgaftman, J. R. Meyer, and L. Ram-Mohan, J. Appl. Phys. **89**, 5815 (2001).

[17] T. L. Alford, L. C. Feldman, and J. W. Mayer, *Fundamentals of Nanoscale Film Analysis* (Springer, Hidelberg, 2007), pp. 43-47.

[18] T. L. Alford, L. C. Feldman, and J. W. Mayer, *Fundamentals of Nanoscale Film Analysis* (Springer, Hidelberg, 2007), pp. 34-39.

[19] Rutherford Backscattering Spectrometry Analysis Package, Genplot, Cortland, OH.

[20] B. D. Cullity, *Elements of X-ray Diffraction* (Addison-Wesley, Reading, 1978), pp. 86-88.

[21] J. Lu, P. T. Webster, S. Liu, Y.-H. Zhang, S. R. Johnson, and D. J. Smith, J. Cryst Growth **425**, 250 (2015).

[22] X'Pert Epitaxy Software, PANalytical B. V., Almelo, The Netherlands.

[23] P. Thompson, D. E. Cox, and J. B. Hastings, J. Appl. Cryst. **20**, 79 (1987).

[24] Z. R. Wasilewski, M. M. Dion, D. J. Lockwood, P. Poole, R. W. Streater, and A. J. SpringThorpe, J. Appl. Phys. **81**, 1683 (1997).

[25] L. Dominguez, D. F. Reyes, F. Bastiman, D. L. Sales, R. D. Richards, D. Mendes, J. P. R. David, and D. Gonzalez, Appl. Phys. Express **6**, 11 (2013).

[26] A. G. Norman, T-Y. Seong, I. T. Ferguson, G. R. Booker, and B. A. Joyce, Semicond. Sci. Technol. **1**, S9 (1993).

[27] A. G. Norman, R. France, and A. J. Ptak, J. Vac. Sci. and Technol. B **29**, 03C121-1 (2011).

[28] T. L. Alford, L. C. Feldman, and J. W. Mayer, *Fundamentals of Nanoscale Film Analysis* (Springer, Hidelberg, 2007), pp. 84-88.

[29] L. Palmetshofer. *Surface and Thin Film Analysis: A Compendium of Principles, Instrumentation and Applications*. Edited by H. B. Gernot Friedbacher, Wiley-VCH Verlag GmbH & Co. KGaA (2011) pp. 191-202.

[30] L. C. Feldman, J. W. Mayer, S. T. Picraux. *Materials Analysis by Ion Channeling*. Academic, New York (1982) pp. 13-20.

[31] H. Okamoto and K. Oe, Jpn. J. Appl. Phys. **38**, 1022 (1999)

[32] L. C. Feldman, J. W. Mayer, S. T. Picraux. *Materials Analysis by Ion Channeling*. Academic, New York (1982) pp. 55-59.

[33] L. C. Feldman, J. W. Mayer, S. T. Picraux. *Materials Analysis by Ion Channeling*. Academic, New York (1982) pp. 76-81.

[34] J. Zhu, S. Oktyabrsky, and M. B. Huang, J. Appl. Phys. **100**, 104312 (2006).

[35] T. Nebiki, T. Narusawa, A. Kumagai, T. Saito, and S. Takagishi, Nucl. Instr. Meth. Phys. Res. B **249**, 501 (2006).

[36] T. Cesca, A. Gasparotto, A. Verna, B. Fraboni, G. Impellizzeri, F. Priolo, L. Tarricone, and M. Longo, Nucl. Instr. Meth. Phys. Res. B **242**, 653 (2006).

[37] S. Imhof, A. Thränhardt, A. Chernikov, M. Koch, N. S. Köster, K. Kolata, S. Chatterjee, S. W. Koch, X. Lu, S. R. Johnson, D. A. Beaton, T. Tiedje, O. Rubel, Appl. Phys. Lett. **96**, 131115 (2010).

[38] C. Gogineni, N. A. Riordan, S. R. Johnson, X. Lu, and T. Tiedje, Appl. Phys. Lett. **103**, 041110, (2013).

[39] P. T. Webster, N. A. Riordan, S. Liu, E. H. Steenbergen, R. A. Synowicki, Y.-H. Zhang, and S. R. Johnson, J. Appl. Phys. **118**, 245706 (2015).

[40] L. Viña, S. Logothetidis, and M. Cardona, Phys. Rev. B **30**, 1979 (1984).

[41] S. R. Johnson and T. Tiedje, J. Appl. Phys. **78**, 5609 (1995).

[42] K. Alberi, J. Wu, W. Walukiewicz, K. M. Yu, O. D. Dubon, S. P. Watkins, C. X. Wang, X. Liu, Y.-J. Cho, and J. Furdyna, Phys. Rev. B **75**, 045203, (2007).

[43] N. A. Riordan, C. Gogineni, S. R. Johnson, X. Lu, T. Tiedje, D. Ding, Y.-H. Zhang, R. Fritz, K. Kolata, S. Chatterjee, K. Volz, and S. W. Koch, J. Mater. Sci. **23**, 1799 (2012).